Research Square

Preprints are preliminary reports that have not undergone peer review.
They should not be considered conclusive, used to inform clinical practice,
or referenced by the media as validated information.

Alkali-Element geochemistry and SWIR spectroscopy and vectors to orogenic gold mineralization in the Pataz Batholith, Peru

Clever Willam Caruajulca-Caruajulca1
Compañia Minera Poderosa
Roy Edinson Coba-Teran
Compañia Minera Poderosa
Carlos Ore-Sanchez
Compañia Minera Poderosa
José Néstor Mamani-Quispe
Universidad Nacional del Altiplano
Jairo Jhonatan Marquina-Araujo
National University of Trujillo
Marco Antonio Cotrina-Teatino
mcotrinat@unitru.edu.pe
National University of Trujillo
Jose Saavedra-Rosas
Curtin University
Salomon Ortiz-Quintanilla
Jorge Basadre Grohmann National University
José A. Guartan
Universidad Técnica Particular de Loja

Research Article

Keywords: orogenic gold, alkali-element geochemistry, SWIR spectroscopy, mineralization vectoring, Pataz Batholith

Posted Date: September 21st, 2026

DOI: https://doi.org/10.21203/rs.3.rs-10910101/v1

License: This work is licensed under a Creative Commons Attribution 4.0 International License.
Read Full License

Additional Declarations: No competing interests reported.

Alkali-Element geochemistry and SWIR spectroscopy and vectors to orogenic gold mineralization in the Pataz Batholith, Peru

Clever Willam Caruajulca-Caruajulca[1], Roy Edinson Coba-Teran[1] , Carlos Ore-Sanchez[1], José Néstor Mamani-Quispe[2], Jairo Jhonatan Marquina-Araujo[3,4], Marco Antonio Cotrina-Teatino[3,4*], Jose Saavedra-Rosas[5], Salomon Ortiz-Quintanilla[6], José A. Guartan[7]

[1]Compañia Minera Poderosa S.A., Lima, Peru.

[2]Department of Chemical Engineering, Faculty of Engineering, National University of Altiplano of Puno, Puno, Peru.

[3]Design and planning of mine - DIPLAMIN research team, Department of Mining Engineering, Faculty of Engineering, National university of Trujillo, Trujillo, Peru.

[4] Research group in Advanced Modeling in Mining (GAMM), Department of Mining Engineering, Faculty of Engineering, National university of Trujillo, Trujillo, Peru.

[5] Minerals and Energy Economics, Curtin University, Curtin, Australia.

[6] Mining Engineering School, Universidad Nacional Jorge Basadre Grohmann, Tacna, Peru.

[7] Department of Mines, Geology and Civil Engineering, Particular Technical University of Loja, Loja, Ecuador

*Corresponding author: Marco Cotrina (mcotrinat@unitru.edu.pe)

Abstract

Deep exploration for orogenic gold veins is hindered by the discontinuous nature of mineralized bodies and the limited vectoring capability of individual indicators. This study evaluated alkali-element geochemistry and short-wave infrared (SWIR) spectroscopy as vectors toward gold mineralization in drill holes DDH11025-074 and DDH11026-081 within the Pataz Batholith, Peru. The integrated dataset comprised geological logging, 1,779 SWIR measurements, Au–Ag and multielement concentrations, the $(Cs + Rb)/Th$, $(Cs + Rb)/Zr$, and $3K/Al$ indices, Spearman rank correlations, and nonparametric statistical tests. In DDH11025-074, the 515.83–587.59 m corridor yielded normalized enrichment values of up to 1.89, 1.82, and 2.24 for the three indices, respectively. Gold exhibited strong positive correlations with white mica ($\rho = 0.816$), As ($\rho = 0.895$), and the geochemical indices ($\rho = 0.711$–0.807). In DDH11026-081, the 523.00–558.88 m domain yielded a median Au concentration of 1.70 ppm, while phengite was positively associated with Au ($\rho = 0.462$). The results demonstrate that the convergence of Cs–Rb and K enrichment, increasing white mica–phengite abundance, decreasing chlorite abundance, and a coupled Au–As response provides a more robust exploration vector than any individual variable. Overall, the integrated geochemical–spectral approach accurately delineates proximal hydrothermal corridors and demonstrates that the combined response of these indicators improves vectoring toward gold mineralization hosted by granitoids, thereby providing a quantitative framework for guiding deep exploration in the Pataz district.

Keywords: orogenic gold; alkali-element geochemistry; SWIR spectroscopy; mineralization vectoring; Pataz Batholith.

1. Introduction

Orogenic gold deposits account for more than 40% of global gold mineralization and occur predominantly within deformed belts associated with crustal-scale faults and shear zones (Y. Wang et al. 2025). Their formation involves the generation, migration, and focusing of hydrothermal fluids through a hierarchy of structural pathways (R. J. Goldfarb et al. 2001). Economically mineralized veins, however, are commonly narrow, discontinuous, and irregularly distributed. Groves et al. (2018) indicated that the largest deposits preferentially occur along second-order structures proximal to regional-scale faults. At the drill-hole scale, however, identifying these structures does not necessarily establish proximity to the mineralizing conduit. This limitation is particularly relevant to deep exploration, where recognizing geochemical and mineralogical halos that extend beyond the veins may substantially reduce drilling uncertainty. In the Mailong orogenic gold deposit, H. Wang et al. (2024) demonstrated that integrating geological mapping with SWIR-derived parameters can identify hydrothermal fluid pathways that remain inconspicuous through conventional observations alone.

Hydrothermal alteration drives mass transfer between fluids and their host rocks. During feldspar destabilization, K, Rb, and Cs may be mobilized and subsequently incorporated into white mica and illite. By contrast, Th and Zr are generally less mobile and may therefore be used as normalizing elements, provided that their stability is independently verified. Heath and Campbell (2004) applied this relationship to propose the $\left((Cs + Rb)/Th\right)_N$ index. In some deposits of the Yilgarn Craton, the halos delineated using this index were 10–100 times more extensive than macroscopically visible alteration. Bacha et al. (2021) confirmed the exploration significance of Rb and Cs at the Pilar and Três Buracos deposits, while also highlighting the influence of protolith composition. The review by Sweetapple et al. (2024) further established that alkali-element lithogeochemical halos may extend over considerable distances; however, their threshold values must be determined locally rather than transferred uncritically among mineralizing systems.

Short-wave infrared (SWIR) reflectance spectroscopy provides a complementary line of evidence because it identifies the mineral phases that record this elemental redistribution. Absorption features associated with Al–OH, Fe–OH, Mg–OH, H_2O, and CO3 enable the discrimination of white mica, chlorite, hydrated clay minerals, and certain carbonate minerals. Meyer et al. (2022) established that the wavelength position of the Al–OH absorption feature near 2200 nm (Pos2200) partly reflects variations in the octahedral composition of white mica. Cloutier et al. (2021), however, demonstrated that this spectral shift is also influenced by interlayer deficiencies, coupled substitutions, and the mixing of mineral phases. At the Canadian Malartic deposit, Gaillard et al. (2018) showed that the compositions of biotite and white mica can distinguish hydrothermal alteration pathways from regional metamorphic trends.

Studies published between 2024 and 2026 indicate that the spectral response of white mica is system-specific. At Xiaonangou, M. Wang et al. (2024) associated Pos2200 values above 2205 nm and higher crystallinity with proximity to gold-bearing bodies. Hao et al. (2024) achieved a classification accuracy of

83.2% using algorithms applied to SWIR parameters from the Tengjia deposit, where Pos2200 values above 2204 nm and a crystallinity index greater than 1.4 characterized mineralized zones. In contrast, H. Wang et al. (2024) recorded shorter wavelengths of 2201–2202.5 nm and crystallinity values ranging from 0.43 to 1.20 near high-grade mineralization at Mailong. These contrasting responses demonstrate that the direction of spectral shifts depends on crystal-chemical substitutions, the physicochemical conditions of the hydrothermal fluid, and the nature of the protolith.

Such variability may also occur within a single district. At Jiaojia, H. Wang et al. (2025) found that Pos2200 lacked a consistent spatial pattern, whereas the crystallinitygggggg index delineated a proximal halo approximately 180–350 m wide. At Jinwozi, Y. Wang et al. (2025) obtained Pos2200 values below 2202.5 nm in three mineralized sectors but documented distinct crystallinity ranges according to host-rock type. Salama et al. (2025) identified relatively Na-rich white mica and Fe-rich chlorite proximal to gold mineralization, in contrast to K-rich mica and Mg-rich chlorite in distal settings. These findings indicate that the most robust vector is not an individual mineral or parameter, but rather a spatially organized mineralogical transition calibrated against independent geochemical evidence.

Similarly, Z. Wang et al. (2026) processed 8,064 spectra from 11 drill holes at the Wuzunbulake orogenic gold deposit and discriminated proximal hydrothermal muscovite from distal metamorphic phengite using Pos2200 and crystallinity. At Kanowna Belle and Sunrise Dam, Y.-H. Liu et al. (2026) combined SWIR spectroscopy with in situ white-mica chemistry and identified significant relationships between Rb/Sr and Cu/Zn ratios and the wavelength position of the Al–OH absorption feature. Zhao et al. (2026) applied partial least squares discriminant analysis and three-dimensional modeling to evaluate SWIR indicators of deep mineralization at Qianchuiliu. Collectively, these studies demonstrate that the predictive capability of SWIR spectroscopy increases when spectral parameters are validated against mineralogical, geochemical, and spatial data.

The study area is located within the Pataz Batholith in the Eastern Cordillera of northern Peru. Its principal intrusive phases were emplaced during the Early Carboniferous, whereas gold mineralization developed subsequently within structural corridors cutting granodioritic, tonalitic, and granitic facies (Haeberlin et al. 2004; Witt et al. 2013). Quartz–carbonate–sulfide veins are controlled by reverse faults, shear zones, and subsidiary structures. Wiemer et al. (2021) demonstrated that the reactivation of inherited structures and strike-slip deformation controlled the geometry, connectivity, and segmentation of mineralized fluid pathways. This structural control explains why high-grade intervals may alternate abruptly with altered rocks displaying only a marginal metal response, thereby limiting the effectiveness of visual indicators when used independently.

Proximal alteration at Pataz comprises sericitization, carbonatization, sulfidation, and silicification, with assemblages containing quartz, white mica, Fe–Mg carbonates, pyrite, and arsenopyrite, together with subordinate galena, sphalerite, and chalcopyrite (Haeberlin et al. 2004; Witt et al. 2016). Witt et al. (2014) observed that some pathfinder elements produce narrow halos, whereas the $\left((Cs + Rb)/Th\right)_N$ index retains a more extensive signature around certain veins. Witt et al. (2016) also identified phengitic white mica associated with specific mineralization styles and transitions toward external chlorite-bearing assemblages.

Nevertheless, these studies did not quantitatively establish whether Cs–Rb redistribution, relative K enrichment, and SWIR mineral assemblages converge spatially toward the same gold-bearing intervals in deep drill holes.

A comparison of the studies most directly related to the research problem is presented in Table 1. Previous investigations have validated either alkali-element geochemistry or spectral indicators across different geological settings, but few have integrated both lines of evidence in granitoid-hosted orogenic gold systems. The scientific problem addressed herein is whether alkali-element redistribution and SWIR-derived mineralogy produce spatially concordant signals of proximity to gold mineralization. The principal challenge is to distinguish a vectoring hydrothermal signature from variations caused by protolith composition, the persistence of primary micas, and barren hydrothermal alteration. Consequently, the isolated occurrence of phengite, muscovite, chlorite, or Rb–Cs enrichment cannot be considered sufficient evidence unless its correspondence with the hydrothermal architecture and Au–Ag distribution is demonstrated. This study aims to evaluate alkali-element geochemistry and SWIR spectroscopy as complementary vectors toward orogenic gold mineralization in the Pataz Batholith. To achieve this objective, geological logging, Au–Ag grades, and mineral assemblages identified using a TerraSpec 4 Hi-Res spectrometer were integrated for drill holes DDH11025-074 and DDH11026-081.

The principal contribution of this study is its drill-hole-scale evaluation of whether three independent responses (alkali-element redistribution, potassic–sericitic enrichment, and SWIR-derived mineralogical zoning) converge toward the same hydrothermal domains. Unlike approaches based on a single mineral or spectral parameter, the proposed model uses spatial continuity and agreement among multiple variables to discriminate distal halos, transitional zones, and proximal domains. This integrated framework provides a reproducible basis for vectoring toward gold mineralization in granitoids of the Pataz Batholith while avoiding the uncritical transfer of spectral thresholds established for other deposits.

2. Geological setting

2.1. Regional geological setting of the Pataz batholith

The study area is located in the Pataz gold district, Pataz Province, La Libertad Region, within the Eastern Cordillera of northern Peru and near the western margin of the Amazonian Craton. **Fig 1** shows its location from the national-scale context to the position of the study area within the Pataz district. Geologically, the area forms part of an intrusive complex elongated along a NNW–SSE trend and emplaced into metamorphic rocks of the Marañón Complex and Neoproterozoic–Paleozoic volcano-sedimentary sequences. The intrusive complex consists predominantly of diorite, tonalite, and granodiorite, with subordinate monzogranitic facies. Zircon U–Pb ages constrain its principal emplacement to approximately 338–336 Ma, whereas ages of approximately 329 Ma indicate that magmatic activity persisted locally during the Mississippian (Witt et al. 2013, 2014).

Table 1. Literature review of studies related to the geochemical and spectral vectoring of gold mineralization

Study	Deposit or geological context	Integrated datasets	Main contribution	Difference from the present study
Heath and Campbell (2004)	Yilgarn Craton, Australia	Whole-rock geochemistry	The $\left((Cs + Rb)/Th\right)_N$ index delineated halos more extensive than macroscopically visible alteration	Did not incorporate SWIR mineralogy
Bacha et al. (2021)	Pilar and Três Buracos, Brazil	Geochemistry and petrography	Rb and Cs recorded hydrothermal alteration, although their distributions were influenced by the protolith	Did not evaluate spectral parameters
Witt et al. (2014)	Pataz goldfield	Geochemistry and reflectance spectroscopy	Identified Rb–Cs dispersion and variations in mica composition	Did not develop a quantitative drill-hole-scale model
Witt et al. (2016)	Northern Pataz	Geology and mineralogy	Identified phengitic mica associated with specific mineralization styles	Did not jointly assess alkali-element indices and Au–Ag distributions
H. Wang et al. (2024)	Mailong, China	Geological mapping, SWIR spectroscopy, and mineralization data	Short-wavelength Pos2200 values and a low crystallinity index delineated gold-bearing fluid pathways	Did not evaluate Cs–Rb indices normalized to Th and Zr
Hao et al. (2024)	Tengjia, China	SWIR spectroscopy and machine learning	Achieved 83.2% accuracy in classifying mineralized samples	The model relied exclusively on spectral parameters
M. Wang et al. (2024)	Xiaonangou, China	SWIR spectroscopy and white-mica chemistry	Long-wavelength Pos2200 values and a high crystallinity index characterized mineralization	Did not incorporate whole-rock alkali-element geochemistry
Salama et al. (2025)	Gold-bearing regolith, Australia	SWIR spectroscopy and mineral chemistry	Na-rich mica and Fe-rich chlorite characterized proximal settings	Focused on weathered material rather than fresh drill core
H. Wang et al. (2025)	Jiaojia, China	SWIR spectroscopy and 3D modeling	The crystallinity index was more effective than Pos2200 for mineralization vectoring	Did not evaluate alkali-element lithogeochemical indices
Y. Wang et al. (2025)	Jinwozi, China	Petrography and SWIR spectroscopy	Spectral responses varied among granite, sandstone, and mylonite	Did not include Cs–Rb–Th–Zr relationships
Z. Wang et al. (2026)	Wuzunbulake, China	8,064 spectra from 11 drill holes	Discriminated hydrothermal muscovite from metamorphic phengite	Did not compare the spectral response with whole-rock geochemical indices
Y.-H. Liu et al. (2026)	Kanowna Belle and Sunrise Dam, Australia	SWIR spectroscopy and in situ mineral chemistry	Related Rb/Sr and Cu/Zn ratios to the Al–OH absorption feature	Requires mineral-scale microanalysis
Present study	Pataz Batholith, Peru	Geological logging, Au–Ag data, multielement geochemistry, and TerraSpec measurements	Evaluates the spatial convergence of alkali-element indices, $3K/Al$, SWIR mineral assemblages, and gold mineralization	Proposes an empirical calibration specifically developed for granitoids of the Pataz Batholith

The regional architecture comprises an uplifted central block exposing the intrusive body, bounded by the Chagual Graben to the west and the Lavasén Graben to the east. As shown in **Fig. 2**, this tectonic configuration is controlled by longitudinal faults predominantly striking NNW–SSE and NW–SE, which are crosscut by NE–SW- to ENE–WSW-trending transverse structures (Witt et al. 2013). Reactivation of inherited basement discontinuities generated fault bends, structural intersections, and dilational zones that locally enhanced permeability and focused hydrothermal fluid flow. Wiemer et al. (2021) demonstrated that the vein-system geometry largely reflects pre-existing basement structures. Subsequently, Wiemer et al. (2022) linked these inherited structural intersections to the clustered spatial distribution of gold deposits in northern Peru.

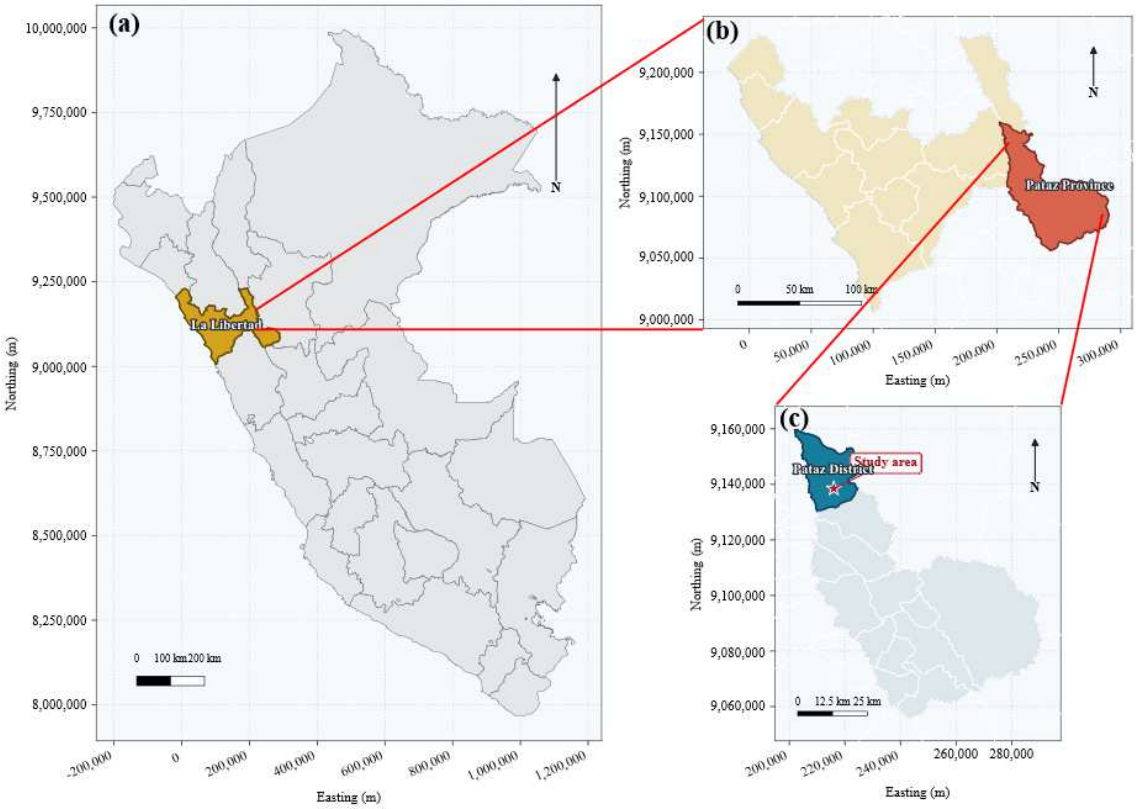


Fig. 1. Geographic location of the study area in northern Peru. (a) Location of the La Libertad Region within Peru; (b) location of Pataz Province within the La Libertad Region; and (c) location of the study area within the Pataz district. Coordinates are expressed in meters using the UTM coordinate system.

The regional configuration is characterized by an uplifted central block bounded by the Chagual Graben to the west and the Lavasén Graben to the east. This architecture is controlled by NNW–SSE- and NW–SE-trending faults segmented by NE–SW- to ENE–WSW-oriented lineaments. Reactivation of inherited basement structures generated structural intersections, fault bends, and dilational zones that promoted hydrothermal fluid migration and the development of mineralized corridors (Wiemer et al. 2021). This structural control also accounts for the clustered distribution of gold-bearing veins and their variable continuity at depth (Wiemer et al. 2022).

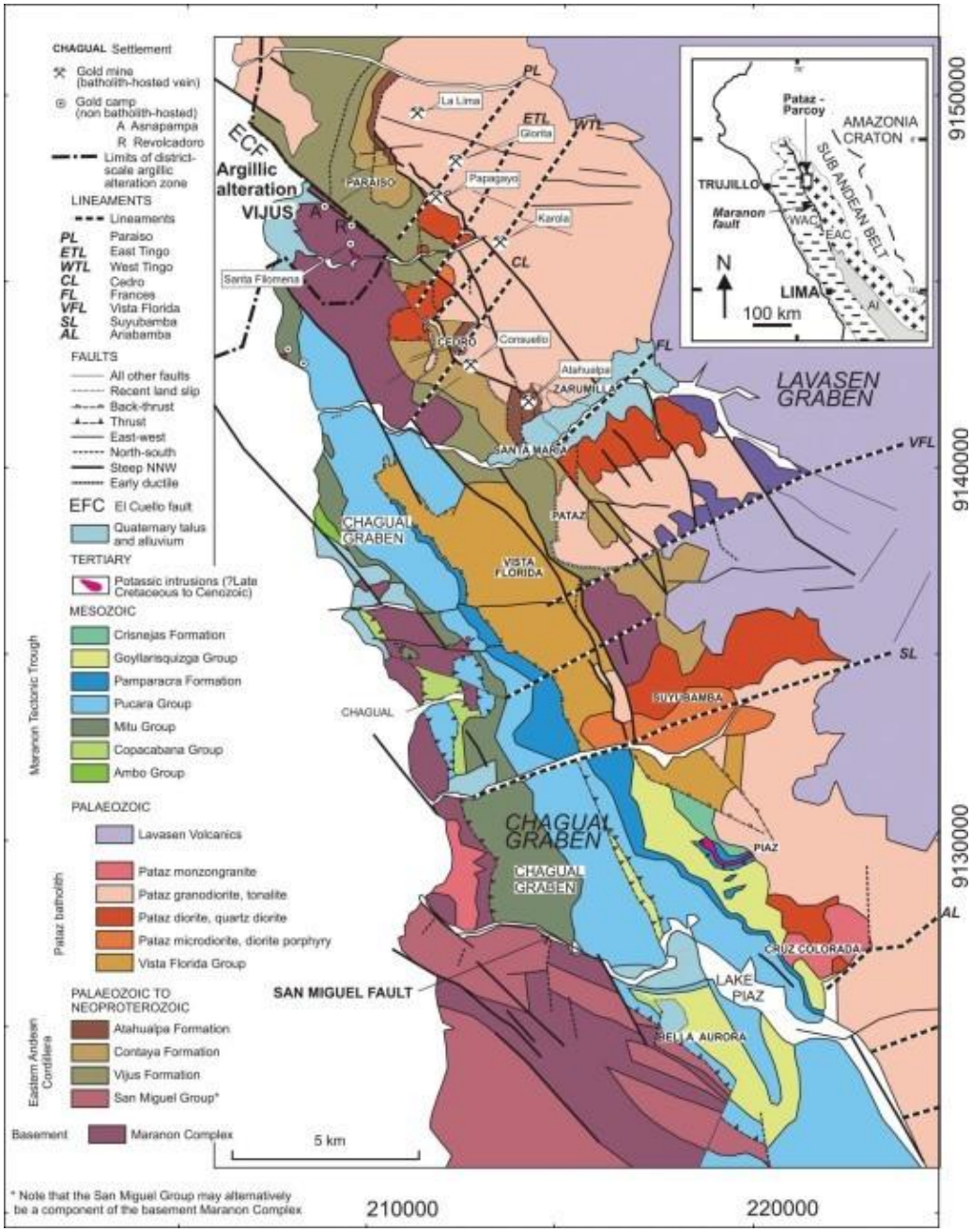


Fig. 2. Geological and structural setting of the Pataz gold district. Modified from Witt et al. (2016).

At the Marañón mining operation, mineralization is hosted predominantly by granodiorite and monzogranite, where it occurs as quartz–carbonate–sulfide veins and veinlets controlled by faults, fractures, and shear zones. The mineralized structures predominantly strike NNW–SSE to NW–SE, although their geometry may vary locally because of branching, changes in strike, and intersections with transverse faults. These features produce substantial variations in vein continuity and thickness, as well as in the distribution of high-grade zones (Haeberlin et al. 2004; Wiemer et al. 2021).

The metallic assemblage is dominated by pyrite and arsenopyrite, accompanied by variable proportions of sphalerite, galena, and chalcopyrite. Gold occurs as free particles or sulfide-related inclusions and, locally, as native gold or electrum along microfractures, grain boundaries, and contacts among quartz, carbonate,

and sulfide minerals (Haeberlin et al. 2004; Witt et al. 2016). Although the system exhibits the defining characteristics of orogenic gold deposits, partly overlapping mineralization styles and hydrothermal assemblages have been identified in northern Pataz, indicating a geological evolution more complex than that of a single-stage vein-forming event (Witt et al. 2016).

Hydrothermal alteration exhibits zoning from outer chlorite–epidote–carbonate assemblages to inner domains characterized by white mica, illite–phengite, Fe–Mg carbonates, silicification, and disseminated sulfides. Proximal to mineralized structures, alteration progressively replaces feldspars and ferromagnesian minerals in the intrusive host rock, accompanied by an increase in white-mica abundance and a relative decrease in epidote and chlorite. However, the isolated occurrence of phengite or muscovite does not necessarily constitute a proximal indicator because these phases may also reflect protolith composition, regional alteration, or superimposed hydrothermal events (Meyer et al. 2022; Witt et al. 2014).

3. Materials and methods

3.1. Study design and methodological workflow

A quantitative, observational study with an exploratory–correlational scope was conducted to evaluate the spatial correspondence among hydrothermal alteration, geochemical signatures, and mineralogy identified through SWIR spectroscopy. The unit of analysis was the drill-core interval, characterized by its depth position, lithology, alteration, mineralization, and available analytical data.

The study included drill holes DDH11025-074 and DDH11026-081, which were selected because they intersect different positions within the structural and hydrothermal corridor. Depth served as the common reference axis for data integration. For DDH11025-074, geological logging, Au–Ag data, multielement geochemistry, lithogeochemical indices, and SWIR mineralogy were integrated. For DDH11026-081, integration was restricted to geological logging, Au–Ag data, and SWIR mineral assemblages because an equivalent multielement dataset was unavailable. This distinction avoided the imputation of missing data and allowed the second drill hole to provide an independent geological, metallogenic, and spectral comparison.

The workflow comprised five stages: (i) drill-hole selection and preliminary delineation of geological intervals; (ii) acquisition, verification, and screening of geochemical and spectral data; (iii) database integration using drill-hole identifiers and depth; (iv) construction of downhole profiles and statistical evaluation; and (v) development of an empirical vectoring model. As summarized in **Fig. 3**, the geochemical and spectral variables were initially processed independently and integrated only after quality-control procedures had been completed. This approach reduced the risk of imposing associations based on a single source of evidence. Combining geological, geochemical, and spectral datasets enables the identification of mineralogical variations that may be difficult to recognize during conventional core logging and facilitates evaluation of their spatial continuity relative to mineralization (Lypaczewski et al. 2019; Medina et al. 2021; Thiele et al. 2024).

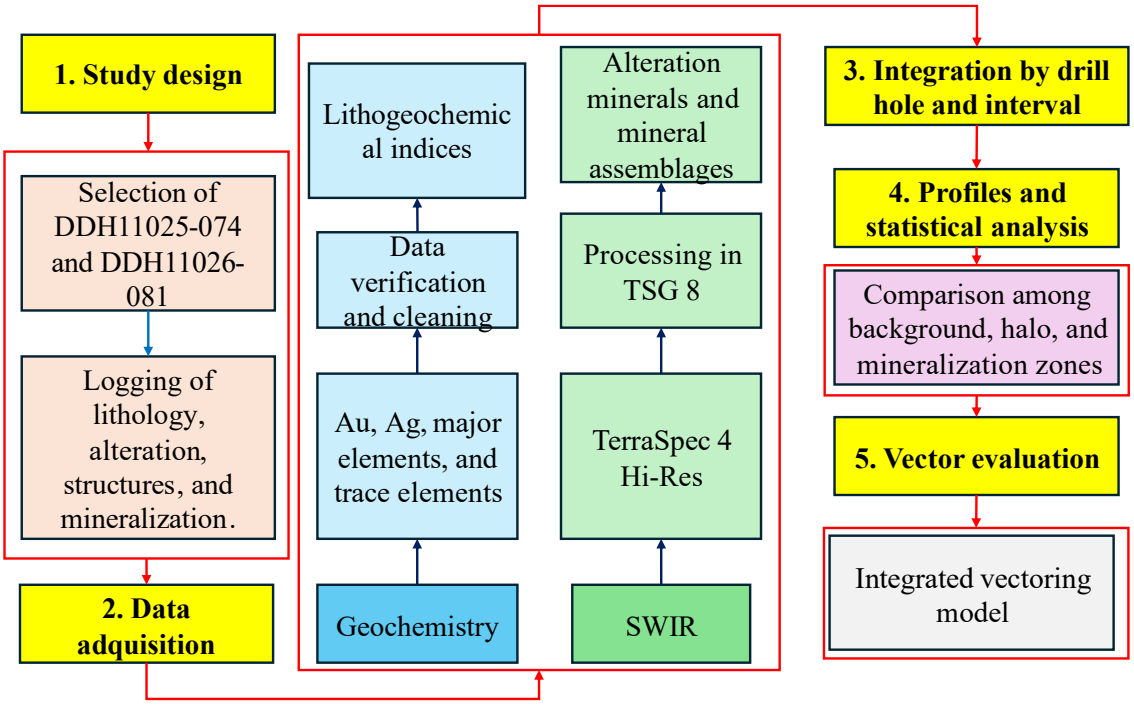


Fig. 3. Methodological workflow for integrating geological, geochemical, and spectral data

3.2. Diamond drill holes and samples selection

In DDH11025-074, the interval from 443.80 to 683.35 m was evaluated, representing 239.55 m of drilled length. In DDH11026-081, the interval from 324.60 to 992.06 m was examined, corresponding to 667.46 m. These lengths represent distances measured along the drill-hole axis rather than the true thicknesses of the intersected structures, as conversion to true thickness requires knowledge of the three-dimensional orientation of each vein relative to the drill-hole trajectory.

Analytical intervals were selected purposively based on changes in lithology, alteration intensity, vein and veinlet frequency, degree of fracturing, sulfide abundance, and proximity to structural contacts. Each record retained the drill-hole identifier and its start and end depths, thereby preserving traceability throughout database integration. For interval-based variables, the midpoint depth was calculated as follows:

$$z_i = \frac{z_{i,start} + z_{i,end}}{2} \quad (1)$$

where z_i represents the position of interval i along the downhole profile, and $z_{i,\mathrm{start}}$ and $z_{i,\mathrm{end}}$ denotes its boundaries in meters.

Interpretation was not based exclusively on individual Au grades. In vein-type deposits, the localized distribution of gold and the potential nugget effect may generate abrupt variations between adjacent samples; consequently, an isolated assay does not necessarily reflect the continuity of the mineralized system (Dominy and Edgar 2012; Dominy et al. 2003). Accordingly, the selection and delineation of domains prioritized the continuity of geological and mineralogical features, whereas Au–Ag concentrations were subsequently used as independent validation variables.

3.3. Geological logging and alteration classification

Drill-core logging included lithology, structural features, vein and veinlet orientations and density, fracture intensity, replacement textures, alteration minerals, and relative sulfide abundance. Lithological, structural, and hydrothermal contacts were delineated by depth and subsequently compared with SWIR mineral identifications. SWIR spectroscopy complemented macroscopic observations, particularly in differentiating white mica, chlorite, and clay minerals displaying similar colors or textures in drill core (Meyer et al. 2022).

Hydrothermal alteration was operationally classified into four domains:

1. Distal: chlorite–epidote–carbonate assemblages.
2. Transitional–proximal: white mica, illite–phengite, and carbonate assemblages.
3. Structural–mineralized: quartz–carbonate assemblages containing pyrite–arsenopyrite and subordinate sulfides.
4. Clay-rich or overprinted: lower-temperature clay minerals, predominantly montmorillonite.

The distinction among distal, proximal, and structural domains was subsequently used to compare the distributions of lithogeochemical indices and SWIR mineral assemblages. Gold concentration was excluded from the classification criteria, thereby avoiding the use of the response variable both to define and subsequently evaluate the groups. This procedure reduces interpretive circularity and enables an independent assessment of whether geochemical and spectral indicators successfully identify mineralized intervals (Gaillard et al. 2018).

Figure 4 documents the principal stages and materials considered in this study, from underground diamond drilling and drill-core organization to spectral acquisition and the identification of hydrothermal structures.

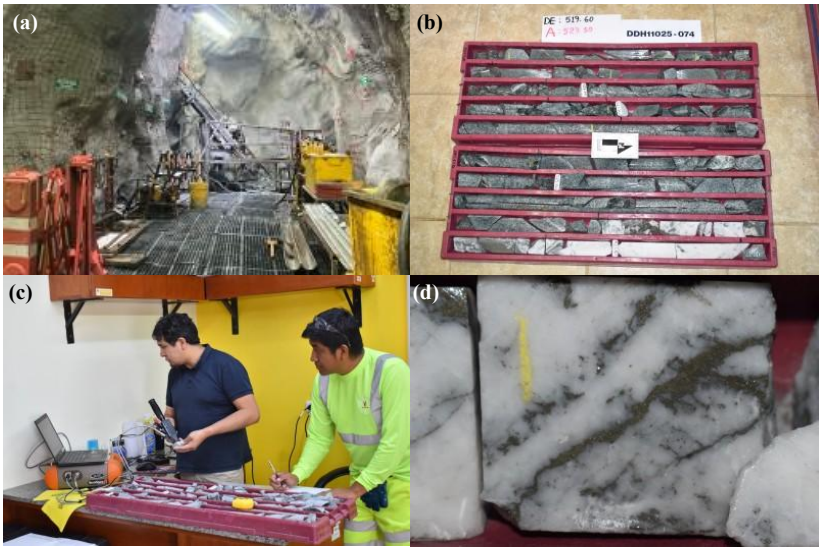


Fig. 4. Materials and characterization of the diamond-drill core. (a) Underground drill platform used for diamond drilling; (b) core boxes from DDH11025-074 corresponding to the 519.60–529.30 m interval; (c) acquisition of drill-core reflectance spectra using a TerraSpec 4 Hi-Res spectrometer; and (d) representative texture of a quartz–carbonate structure containing visible sulfides.

3.4. Sample preparation and geochemical analysis

Au and Ag concentrations were obtained from laboratory-certified analytical results. Major and trace elements were determined by four-acid digestion followed by instrumental analysis using ICP–AES or ICP–MS, depending on the analytical method commissioned. Digestion with HNO3–HClO4–HF followed by final dissolution in HCl provides near-total recovery for many minerals; however, refractory phases such as zircon, chromite, barite, and certain oxides may be incompletely recovered (ALS Global 2023). Accordingly, Th and Zr were treated as comparatively immobile reference elements, but not as absolutely immobile or quantitatively recovered in every sample.

The geochemical dataset for DDH11025-074 comprises 72 intervals with analytical results for Au, Ag, Cs, Rb, K, Th, Zr, and Al, together with As, Cu, Pb, and Zn as auxiliary elements. DDH11026-081 contains Au–Ag data and SWIR mineralogical information but lacks the multielement dataset required to calculate alkali-element indices. Consequently, the lithogeochemical indices and their correlations were evaluated exclusively for DDH11025-074.

Au concentrations reported in ppb were converted to ppm as follows:

$$Au_{ppm} = \frac{Au_{ppb}}{1000} \tag{2}$$

Elements reported as weight percentages were converted to ppm, where necessary, using:

$$C_{ppm} = C_{\%} * 10^4 \tag{3}$$

Before data processing, sample identifiers, interval continuity and potential overlap, measurement units, missing values, analytical qualifiers, and detection limits were verified. Results below the detection limit were not treated as zero. For numerical analyses, these values were replaced with one-half of the detection limit ($DL/2$) while retaining their classification as censored observations. In the Spearman correlation analyses, these observations were assigned tied ranks, thereby avoiding the introduction of an artificial ordering among non-quantified concentrations. Because 18 of the 72 Au values and 26 of the 72 Ag values in DDH11025-074 occurred at the minimum reported detection limit, censoring frequencies were reported together with the descriptive statistics.

3.5. SWIR spectral acquisition

Spectra were acquired directly from the drill core using a portable ASD TerraSpec 4 Hi-Res spectrometer. The instrument records reflectance across 2,151 channels over the 350–2500 nm wavelength range, with spectral resolutions of 3 nm at 700 nm and 6 nm at 1400 and 2100 nm, a wavelength accuracy of 0.5 nm, and a wavelength reproducibility of 0.1 nm. This spectral range enables the identification of absorption features associated with Al–OH, Fe–OH, Mg–OH, H_2O, and CO_3, which are characteristic of white mica, chlorite, hydrated clay minerals, and certain carbonate minerals (Meyer et al. 2022).

Measurements were collected from clean and representative surfaces, avoiding open fractures, coatings, surface moisture, and locations where contact between the probe and drill core was inadequate. Measurement density was increased across veins, contacts, and intensely altered zones, whereas wider

spacing was used in relatively homogeneous host rock. Multiple measurements were collected at selected depths to characterize mineralogical heterogeneity at the centimeter scale. An integration time of 5 s was used for each measurement.

A total of 1,670 spectral records were obtained from DDH11025-074 and 109 from DDH11026-081. Each spectrum retained its ASD file identifier, drill-hole code, and downhole position. Owing to differences in coverage and analytical structure between the datasets, individual spectra were not treated as independent geochemical observations. Instead, spectra were first grouped within their corresponding sample intervals, after which mineralogical frequencies were calculated to avoid statistical pseudoreplication.

The analytical coverage used for data integration is summarized in **Table 2**.

Table 2. Geochemical and spectral coverage of the investigated drill holes

Drill hole	Evaluated interval (m)	Geochemical intervals	SWIR records	Available variables
DDH11025-074	443.80 – 683.35	72	1670	Au–Ag, multielement geochemistry, lithogeochemical indices, mineralogy, and SWIR parameters
DDH11026-081	324.60 – 992.06	-	109	Au–Ag and SWIR mineral assemblages

3.6. Spectral processing and interpretation

Spectra were processed using The Spectral Geologist 8 (TSG 8) and linked to their respective acquisition depths. Mineral identification was performed through automated matching against spectral libraries, followed by a consistency review against the material observed in the drill core. Records classified as aspectral, null identifications, spectra with insufficient spectral response, and assignments incompatible with the observed mineralogy or texture were excluded. Combining automated filtering with geological review reduces the propagation of spurious spectral classifications in extensive drill-core datasets (Thiele et al. 2024).

The fitting coefficients reported by uTSAS or sTSAS were used to identify the dominant mineral and secondary components but were not interpreted as absolute modal abundances (L. Liu et al. 2024). For DDH11025-074, the processed dataset included the wavelength position and band depth of the Al–OH absorption feature, the Fe–OH wavelength position, and the estimated spectral abundance of white mica. The Al–OH wavelength position (Pos2200) was available for 68 of the 72 intervals, whereas white-mica abundance was available for 69 intervals. These parameters were used quantitatively after verifying their ranges, downhole continuity, and mineralogical associations. For DDH11026-081, only mineral assignments and their relative weights were retained because the dataset lacked equivalent quantitative band parameters. Consequently, Pos2200 was not directly compared between the two drill holes.

Each SWIR measurement was assigned to the geochemical interval containing its acquisition depth:

$$From_i \leq d_s < To_i \tag{4}$$

where d_s is the Depth of the spectral measurement, and $From_i$ and To_i denote the boundaries of geochemical interval i.

When an interval contained more than one valid measurement, the relative frequency of mineral assemblage m was calculated as follows:

$$P_{m,i} = \frac{n_{m,i}}{N_i} * 100 \tag{5}$$

where $n_{m,i}$ is the number of measurements in which mineral assemblage m, and N_i is the total number of valid spectra within interval i. Intervals lacking SWIR coverage were retained as missing data and were not interpolated.

3.7. Calculation of lithogeochemical indices

The lithogeochemical indices were recalculated from the original analytical concentrations of Cs, Rb, Th, Zr, K, and Al.

3.7.1. Normalized $[(\boldsymbol{Cs} + \boldsymbol{Rb})/\boldsymbol{Th}]_N$ *index*

For each interval in DDH11025-074, the following ratio was calculated:

$$R_i = \frac{Cs_i + Rb_i}{Th_i} \tag{6}$$

The local background was defined using samples from the same granitoid unit that jointly met the following criteria: absence of quartz–sulfide veins, weak visually observed alteration, low veinlet density, and absence of a dominant proximal white-mica assemblage. Au concentration was not used to select background samples. Owing to the limited sample size and skewed distribution of the geochemical ratios, the background value was estimated using the median:

$$R_{bg} = \frac{1}{n_{bg}} \sum_{j=1}^{n_{bg}} \left(\frac{Cs_j + Rb_j}{Th_j} \right), j \in BG \tag{7}$$

where BG denotes the set of samples used to define the local background. The normalized ratio was then calculated as follows:

$$\left[\frac{Cs + Rb}{Th} \right]_{N,i} = \frac{R_i}{R_{bg}} \tag{8}$$

A value of 1 represents a response equivalent to the local background, whereas values above or below 1 indicate relative enrichment or depletion, respectively. The index was interpreted as a continuous variable rather than according to a universal threshold (Bacha et al. 2021; Heath and Campbell 2004).

3.7.2. $(\boldsymbol{Cs} + \boldsymbol{Rb})/\boldsymbol{Zr}$ *index*

The following ratio was calculated as an independent comparator:

$$I_{CsRb/Zr,i} = \frac{Cs_i + Rb_i}{Zr_i} \quad (9)$$

The index is dimensionless when all three elements are expressed in ppm. Unscaled values were used in the analyses. Because Zr concentrations may vary with zircon abundance and intrusive facies, the ratio was interpreted within comparable lithological units and in conjunction with the Th-normalized index, rather than as an absolute measure of alteration.

3.7.3. Molar $3K/Al$ index

The K and Al concentrations, expressed in the same mass units, were converted to molar quantities:

$$K_{mol,i} = \frac{K_i}{39.0983} \quad (10)$$

$$Al_{mol,i} = \frac{Al_i}{26.9815} \quad (11)$$

The molar index was subsequently calculated as follows:

$$I_{3K/Al,i} = \frac{3K_{mol.i}}{Al_{mol,i}} = 3\left(\frac{K_i/39.0983}{Al_i/26.9815}\right) \quad (12)$$

This dimensionless index represents the molar enrichment of K relative to Al. Its interpretation was evaluated against white-mica frequency, Pos2200, and Al–OH absorption-band depth. Although a value approaching 1 may be consistent with an ideal white-mica-dominated composition, the index may also be influenced by K-feldspar, biotite, and lithological variability. It was therefore not used as independent evidence of sericitization.

3.8. Data integration and statistical analysis

Data integration was performed using the drill-hole identifier and downhole position. The analytical interval, rather than each individual spectrum, was treated as the statistical unit. When an interval contained multiple SWIR measurements, these were summarized using mineral-assemblage frequencies and the median values of quantitative spectral parameters. This procedure prevented intervals with a greater density of spectral measurements from receiving disproportionate statistical weight.

Continuous variables were summarized using the number of valid observations, median, interquartile range, minimum, maximum, and 10th and 90th percentiles. The frequency of censored observations was reported for Au and Ag. For graphical representation, Au, Ag, As, Cu, Pb, and Zn were displayed on logarithmic scales, whereas all statistical analyses were performed using the original concentration values.

For DDH11025-074, monotonic associations among Au, Ag, As, Cu, Pb, Zn, $[(Cs + Rb)/Th]_N$, $(Cs + Rb)/Zr$, $3K/Al$, Pos2200, Al–OH band depth, and white-mica frequency were evaluated using Spearman's rank correlation coefficient. Because tied values were present, the coefficient was calculated as the Pearson correlation applied to ranked data:

$$\rho_s = \frac{cov(R_X, R_Y)}{\sigma_{R_X}\sigma_{R_Y}} \tag{13}$$

where R_X and R_Y represent the ranks of the variables being compared. The reported statistics included ρ_s, the p-value, the number of valid pairs, and the 95% confidence interval. The p-values from the correlation matrix were adjusted using the Benjamini–Hochberg procedure to control the false discovery rate.

For DDH11026-081, correlations involving lithogeochemical indices were not calculated; the analysis was restricted to Au–Ag data and comparisons of grades among SWIR mineral assemblages. Differences among the distal, transitional–proximal, structural–mineralized, and clay-rich domains were evaluated using the Kruskal–Wallis test. The test statistic was calculated as:

$$H = \frac{12}{N(N+1)}\sum_{g=1}^{k}\frac{R_g^2}{n_g} - 3(N+1) \tag{14}$$

where R_g is the sum of ranks for group g, n_g is the number of observations in that group, k is the number of groups, and N is the total number of observations. When the overall test was significant, Dunn's post hoc pairwise comparisons with Holm adjustment were performed. Effect size was estimated as:

$$\varepsilon^2 = \frac{H - k + 1}{N - k} \tag{15}$$

A significance level of $\alpha = 0.05$was adopted. Missing observations were excluded on a pairwise basis and were neither imputed nor interpolated.

4. Results

4.1. Geological and hydrothermal architecture of the drill holes

Integration of geological logging and spectral mineralogy enabled the delineation of hydrothermal domains with distinct mineral compositions and degrees of spatial continuity. DDH11025-074 contains 1,670 SWIR records distributed almost continuously between 443.80 and 683.35 m. In contrast, DDH11026-081 contains 109 records concentrated within specific intervals between 324.60 and 992.06 m. Table 3 summarizes the boundaries, spectral coverage, and mineral assemblages of each domain.

4.1.1. Hydrothermal architecture of DDH11025-074

The 443.80–515.69 m interval corresponds to the distal halo and contains 534 valid spectra. Fe–Mg chlorite accounts for 78.3% of the primary mineral identifications, followed by muscovite (11.4%), phengite (3.4%), and epidote (2.1%). Between 515.83 and 539.70 m, Fe–Mg chlorite decreases to 23.8%, whereas muscovite and phengite increase to 42.4% and 19.8%, respectively. The appearance of ankerite and siderite as secondary phases marks the transition toward a white-mica–Fe–Mg-carbonate assemblage.

407 **Table 3.** Hydrothermal domains and spectral coverage of drill holes DDH11025-074 and DDH11026-081

Drill hole	Interval (m)	Drilled length (m)	Hydrothermal domain	SWIR spectra, n	Dominant mineral	Characteristic mineral assemblage
DDH11025-074	443.80–515.69	71.89	Distal halo	541	Fe–Mg chlorite, 77.8%	Fe–Mg chlorite–muscovite–epidote–calcite
DDH11025-074	515.83–539.70	23.87	Proximal transition	177	Muscovite, 42.0%	Muscovite–phengite–chlorite–ankerite–siderite
DDH11025-074	539.84–587.59	47.75	Central hydrothermal domain	302	Fe–Mg chlorite, 39.5%	Muscovite–phengite–illite–chlorite
DDH11025-074	587.73–635.47	47.74	Chlorite halo	319	Fe–Mg chlorite, 80.3%	Fe–Mg chlorite–muscovite
DDH11025-074	635.61–683.35	47.74	Peripheral halo	327	Fe–Mg chlorite, 49.8%	Fe–Mg chlorite–muscovite–muscovitic illite–calcite
DDH11026-081	324.60–330.53	5.93	Shallow hydrothermal domain	14	Phengite, 77.8%	Phengite–siderite–montmorillonite
DDH11026-081	330.53–523.00	192.47	Distal–transitional domain	18	Phengite, 60.0%	Phengite–siderite–montmorillonite–magnesite
DDH11026-081	523.00–558.88	35.88	Main hydrothermal domain	53	Phengite, 92.5%	Phengite–ankerite–magnesite
DDH11026-081	558.88–686.40	127.52	Chlorite halo	14	Fe–Mg chlorite, 50.0%	Fe–Mg/Fe chlorite–muscovite–phengite
DDH11026-081	686.40–969.52	283.12	Intermediate structural domain	2	Phengitic illite, 100%	Phengitic illite–siderite
DDH11026-081	969.52–969.62	0.1	Deep microdomain	3	Siderite, 100%	Siderite–Fe chlorite–montmorillonite
DDH11026-081	969.62–992.06	22.44	Basal domain	5	Phengite, 60.0%	Phengite–muscovitic illite–Mg chlorite

408

The central hydrothermal domain extends from 539.84 to 587.59 m. Among its 297 valid spectra, Fe–Mg chlorite accounts for 39.7% of the primary mineral identifications, muscovite for 27.3%, phengite for 12.8%, muscovitic illite for 12.5%, and phengitic illite for 5.1%. The combined distribution of these phases distinguishes this domain from the outer chlorite-dominated intervals, even though no individual mineral accounts for more than 40% of the primary identifications.

Below 587.73 m, Fe–Mg chlorite becomes dominant again. It accounts for 80.3% of the identifications within the 587.73–635.47 m interval and decreases to 50.0% between 635.61 and 683.35 m, where muscovite and muscovitic illite increase to 32.4% and 14.8%, respectively. The simplified downhole mineralogical sequence is:

$$Chlorite - epidote \rightarrow muscovite - phengite - carbonate \rightarrow white\ mica - illite - chlorite \rightarrow chlorite - muscovite - calcite$$

This sequence delineates a 47.75-m-wide central domain preceded by a 23.87-m transitional zone and bounded by predominantly chlorite-bearing assemblages.

4.1.2. Hydrotermal architecture of DDH11026-081

The shallow 324.60–330.53 m interval contains nine mineralogically valid spectra. Phengite is the dominant mineral in seven records (77.8%), whereas siderite dominates two (22.2%); montmorillonite occurs as a secondary component. Between 330.53 and 523.00 m, 15 valid spectra were identified, dominated by phengite (60.0%) and siderite (33.3%). Given their low sampling density across the 192.47-m-long interval, these identifications represent isolated observations rather than continuous spectral coverage.

The main hydrothermal domain is concentrated between 523.00 and 558.88 m and contains 53 valid spectra. Phengite dominates 49 records (92.5%), whereas phengitic illite accounts for the remaining 7.5%. Ankerite and magnesite occur as secondary phases. Immediately below this domain, between 558.88 and 686.40 m, Fe–Mg chlorite increases to 50.0%, accompanied by phengite (28.6%), Fe chlorite (14.3%), and siderite (7.1%).

Spectral coverage decreases markedly below 686.40 m. The 686.40–969.52 m interval is represented by two phengitic-illite identifications; the 969.52–969.62 m microdomain contains three siderite identifications accompanied by Fe chlorite and montmorillonite; and the basal 969.62–992.06 m interval contains three phengite and two muscovitic-illite identifications. The observed downhole sequence can therefore be summarized as:

$$phengite - siderite \rightarrow phengite - carbonate \rightarrow chlorite - phengite \rightarrow phengitic\ illite/siderite$$

The spatial continuity of the final two assemblages remains poorly constrained because of the limited spectral coverage.

4.1.3. Comparison between the drill holes

DDH11025-074 has dense spectral coverage and displays a progressive transition from chlorite-dominated assemblages to a white-mica–illite domain, followed by a return to chlorite-dominated conditions. In DDH11026-081, 53 of the 109 spectral records (48.6%) are concentrated between 523.00 and 558.88 m, whereas the extensive 686.40–969.52 m interval contains only two measurements. Therefore, the apparent segmentation of the second drill hole must be interpreted in light of this uneven sampling distribution. The comparative hydrothermal architecture is presented in **Figs. 5** and **6**.

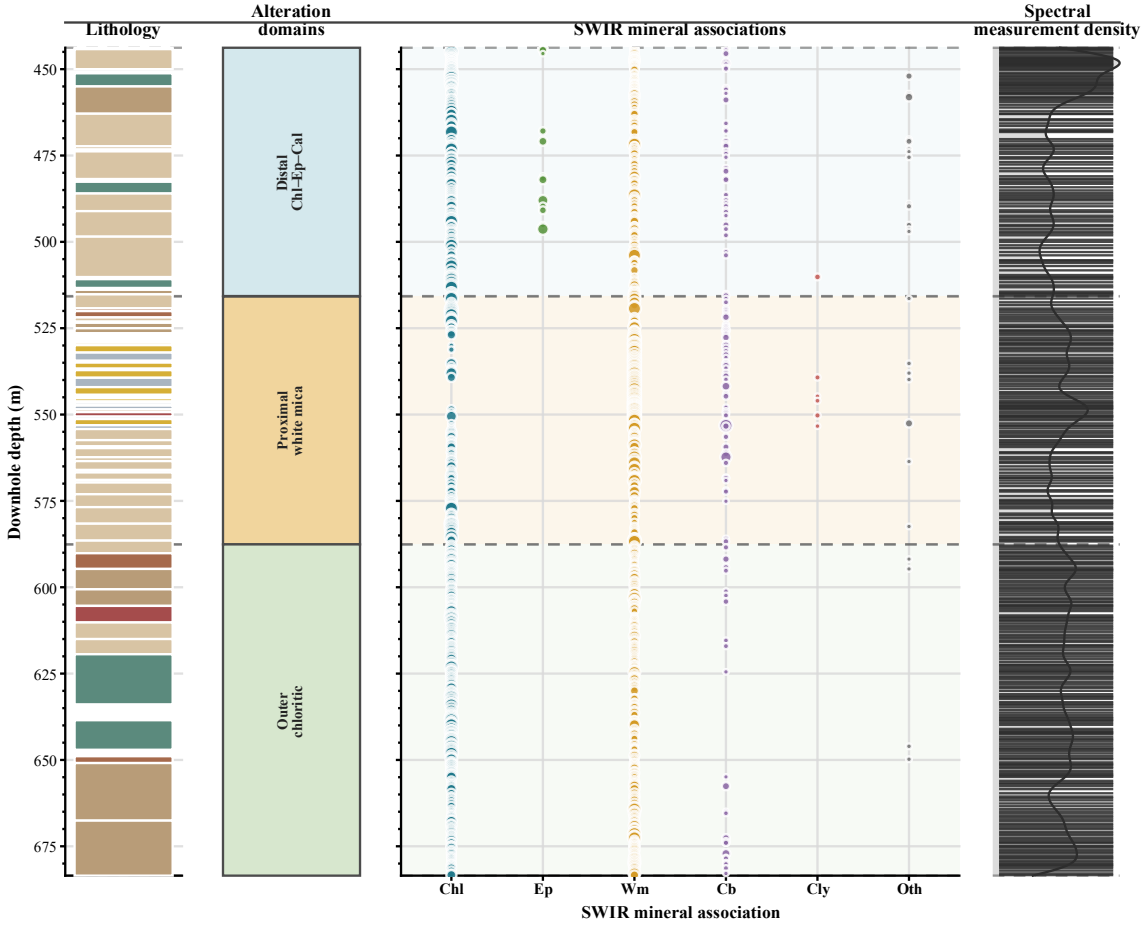


Fig. 5. Downhole distribution of hydrothermal domains and SWIR mineral assemblages in DDH11025-074

4.2. Distribution of Au-Ag and associated elements

The geochemical profiles reveal two contrasting metal-distribution patterns. In DDH11025-074, enrichment is concentrated between 515.83 and 587.59 m and comprises a series of high-grade peaks followed by a broader interval with persistently elevated Au and As concentrations. In DDH11026-081, the Au–Ag distribution is discontinuous and includes a shallow domain, a principal interval between 523.00 and 558.88 m, and a discrete anomaly at 969.52–969.62 m.

The distributions of Au, Ag, As, Cu, Pb, and Zn across the hydrothermal domains of DDH11025-074 are presented in **Table 4**. Pb and Zn values encoded as 10,001 ppm in the database are reported as > 10,000

ppm because they represent concentrations exceeding the upper limit of quantification rather than exact analytical values. For DDH11026-081, **Table 5** presents the Au–Ag concentrations and the Ag/Au ratio calculated separately for each interval. Summary statistics were derived from 44 independent samples.

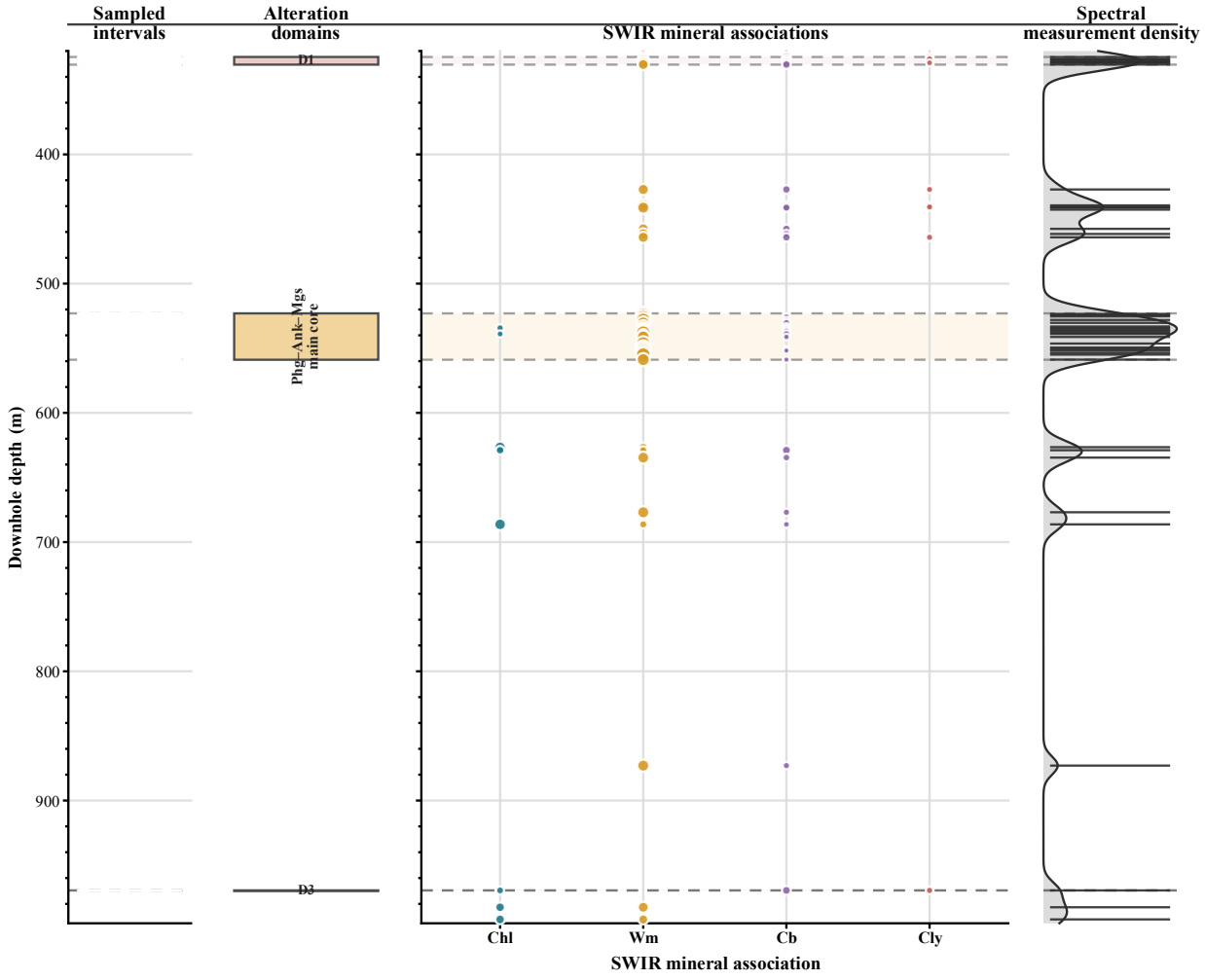


Fig. 6. Downhole distribution of hydrothermal domains and SWIR mineral assemblages in DDH11026-081

4.3. Metal distribution in DDH11025-074

Between 443.80 and 515.69 m, metal concentrations remain close to the local background. Au has a median concentration of 0.0025 ppm and a maximum of 0.007 ppm, whereas As, Cu, Pb, and Zn have median concentrations of 2.5, 2.4, 3.9, and 40.0 ppm, respectively. Enrichment begins within the 515.83–539.70 m proximal transition. The median Au concentration increases to 0.339 ppm, approximately 136 times the distal median, while Ag reaches a median of 0.510 ppm. The highest Au concentration in the drill hole (31.20 ppm) occurs between 528.18 and 528.60 m. Maximum Ag and Cu concentrations of 59.50 and 101 ppm, respectively, occur between 529.21 and 529.91 m, whereas the maximum As concentration (2,870 ppm) occurs between 534.44 and 534.95 m. Although these maxima do not occur within a single sample, they are concentrated within an approximately 7-m-long interval.

Table 4. Au, Ag, and associated-element concentrations by hydrothermal domain in DDH11025-074

Domain	(n)	Au, median; maximum (ppm)	Ag, median; maximum (ppm)	As, median; maximum (ppm)	Cu, median; maximum (ppm)	Pb, median; maximum (ppm)	Zn, median; maximum (ppm)
Distal halo	15	0.0025; 0.007	0.005; 0.10	2.5; 6.7	2.4; 11.7	3.9; 10.2	40.0; 67
Proximal transition	19	0.339; 31.20	0.510; 59.50	80.2; 2870	10.5; 101	114.0; 1680	176.5; 9010
Central domain	26	0.419; 9.18	0.070; 11.45	158.8; 1885	5.45; 68.3	10.6; 5340	58.0; 3950
Chlorite halo	8	0.0095; 0.147	0.005; 0.005	1.05; 6.7	1.65; 20.7	3.6; 15.4	38.0; 97
Peripheral halo	4	0.0038; 0.008	0.005; 0.005	1.4; 2.3	1.85; 3.7	3.0; 3.4	41.5; 85

Note. n denotes the number of independent analytical intervals. Values below the detection limit were represented by one-half of the detection limit ($DL/2$).

Table 5. Distribution of Au–Ag and Ag/Au ratios by hydrothermal domain in DDH11026-081

Domain	Interval (m)	(n)	Au, median [IQR]; maximum (ppm)	Ag, median [IQR]; maximum (ppm)	Median Ag/Au
Shallow domain	324.60–330.53	7	0.750 [0.300–2.415]; 4.00	2.70 [2.26–4.54]; 6.00	3.60
Distal-transitional domain	330.53–523.00	8	0.350 [0.300–0.438]; 0.60	5.03 [4.93–5.08]; 5.95	14.43
Main gold-bearing domain	523.00–558.88	19	1.70 [1.10–2.38]; 6.80	6.30 [5.78–6.85]; 7.95	4.03
Chlorite halo	558.88–686.40	6	0.625 [0.263–0.950]; 1.55	3.30 [3.25–3.54]; 9.70	8.11
Intermediate domain	686.40–969.52	1	0.350; 0.350	8.70; 8.70	24.86
Deep anomaly	969.52–969.62	1	3.10; 3.10	60.20; 60.20	19.42
Basal domain	969.62–992.06	2	0.225 [0.188–0.263]; 0.30	3.98 [3.11–4.84]; 5.70	17.00

Note. n denotes the number of independent analytical intervals; IQR, interquartile range. Values below the detection limit were represented in the processed dataset by one-half of the corresponding detection limit.

The 539.84–587.59 m central domain has a median Au concentration of 0.419 ppm and a maximum of 9.18 ppm. Although its maximum is lower than that of the proximal transition, its median is slightly higher. Arsenic reaches a median concentration of 158.8 ppm and a maximum of 1,885 ppm. Cu, Pb, and Zn also exhibit localized enrichment, including Pb and Zn concentrations exceeding 10,000 ppm. Below 587.73 m, the metal response decreases markedly. Median Au declines to 0.0095 ppm in the chlorite halo and 0.0038 ppm in the peripheral halo. Median As decreases to 1.05 and 1.4 ppm, respectively, whereas Cu, Pb, and Zn return to concentrations similar to those recorded in the distal halo. Overall, DDH11025-074 contains two contiguous geochemical expressions: a proximal interval characterized by closely clustered Au–Ag–As–Cu–Pb–Zn maxima and a broader central domain distinguished by persistently elevated Au and As concentrations (**Fig. 7**).

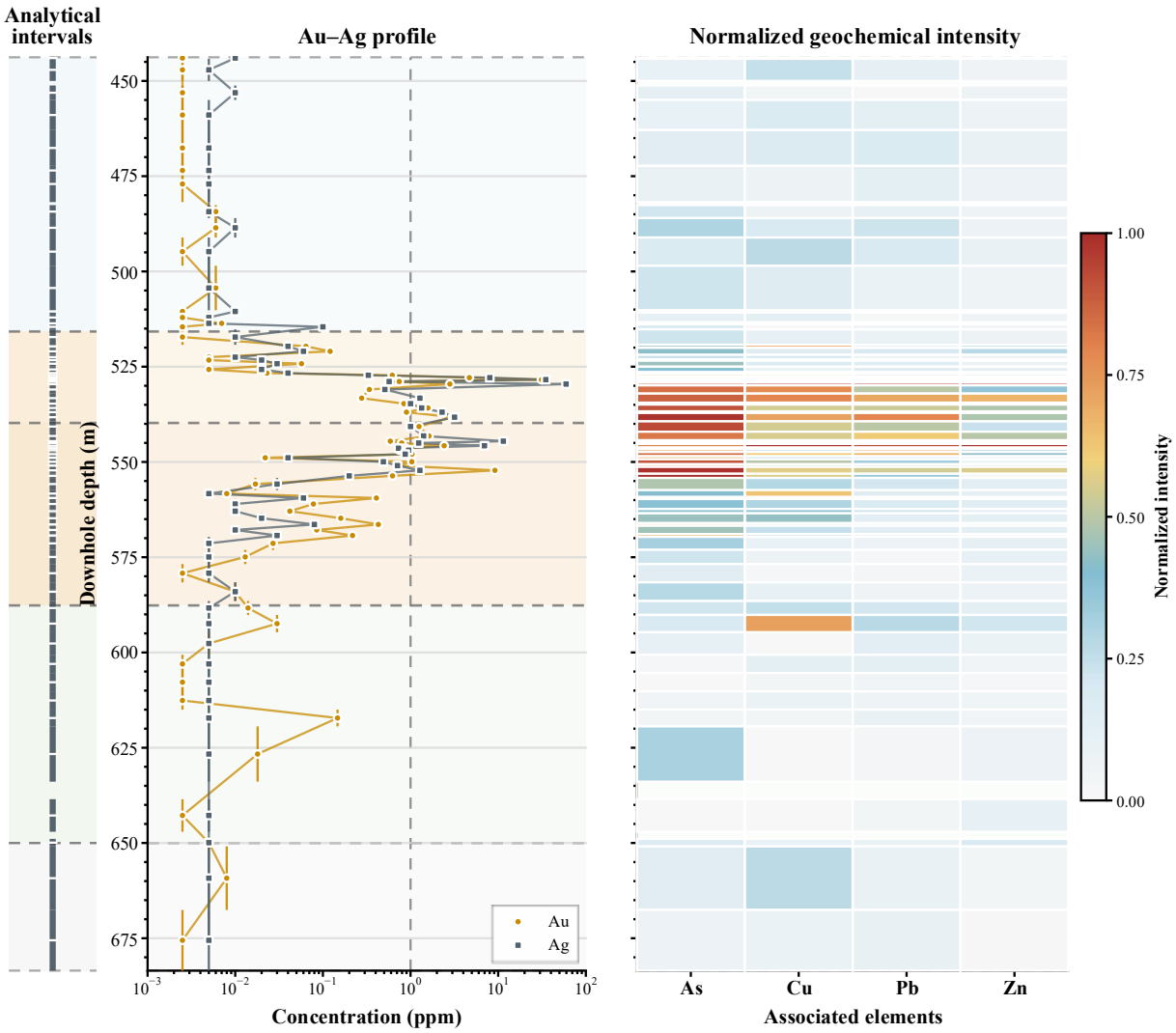


Fig. 7. Downhole distribution of Au–Ag and associated elements in DDH11025-074

4.4. Au-Ag distribution in DDH11026-081

The shallow 324.60–330.53 m domain has a median Au concentration of 0.750 ppm, an IQR of 0.300–2.415 ppm, and a maximum of 4.00 ppm. Ag has a median concentration of 2.70 ppm and a maximum of 6.00 ppm. The wide Au IQR indicates considerable variability among the seven samples from this interval.

Between 330.53 and 523.00 m, median Au decreases to 0.350 ppm, whereas Ag maintains a median concentration of 5.03 ppm. The median Ag/Au ratio increases from 3.60 in the shallow domain to 14.43 in the distal–transitional domain.

The main 523.00–558.88 m domain comprises 19 intervals and exhibits the most continuous gold enrichment in the drill hole. Au reaches a median concentration of 1.70 ppm, an IQR of 1.10–2.38 ppm, and a maximum of 6.80 ppm. Ag has a median concentration of 6.30 ppm, an IQR of 5.78–6.85 ppm, and a maximum of 7.95 ppm. Median Au is 4.9 times higher than in the preceding domain, whereas the median Ag/Au ratio decreases to 4.03.

Within the 558.88–686.40 m chlorite halo, median Au decreases to 0.625 ppm, although it locally reaches 1.55 ppm. Ag has a median concentration of 3.30 ppm and a maximum of 9.70 ppm. The median Ag/Au ratio increases to 8.11 and exhibits a wide interquartile range, reflecting the variability among the six samples.

The intermediate domain is represented by a single sample containing 0.35 ppm Au and 8.70 ppm Ag. The most Ag-rich anomaly occurs at 969.52–969.62 m and contains 3.10 ppm Au and 60.20 ppm Ag, with an Ag/Au ratio of 19.42. Because this result corresponds to a 0.10-m-long sample, it defines a discrete anomaly and does not demonstrate vertical continuity. The two samples from the basal domain have median concentrations of 0.225 ppm Au and 3.98 ppm Ag (**Fig. 8**).

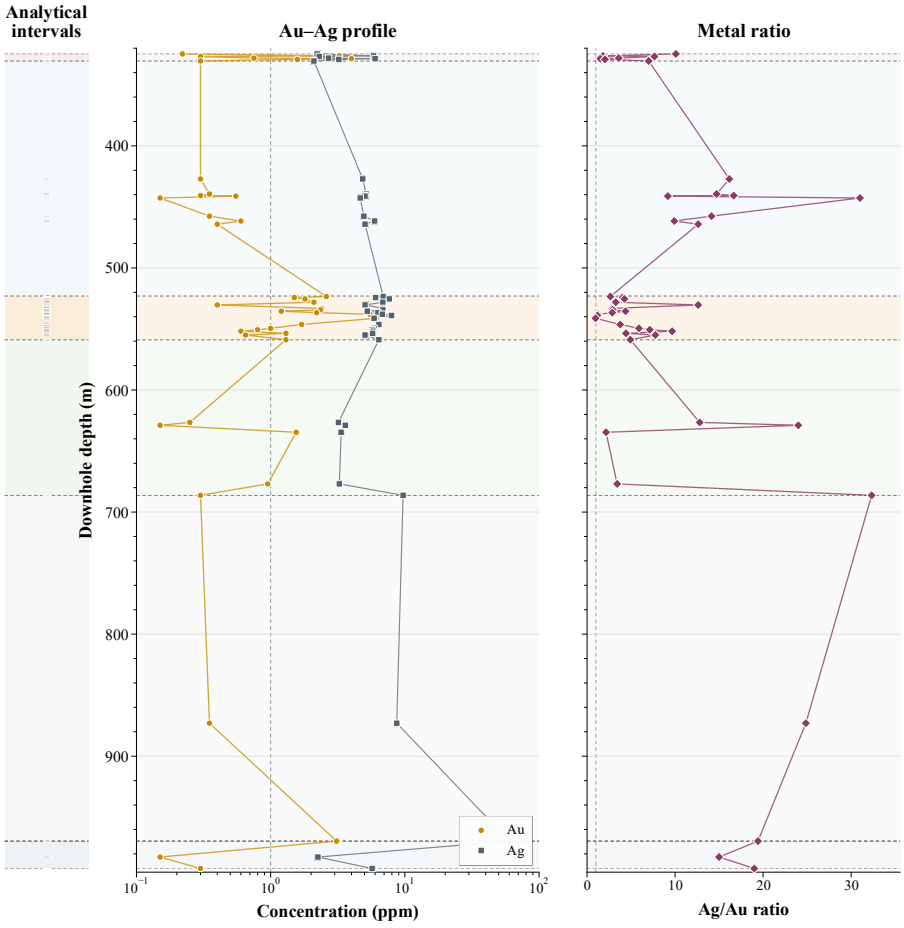


Fig. 8. Downhole distribution of Au–Ag and associated elements in DDH11026-081

519 **4.5. Behavior of the lithogeochemical indices**

520 The lithogeochemical indices were evaluated exclusively for the 72 analytical intervals in DDH11025-074.
521 Normalization was performed relative to the median values of the distal halo: 7.135 for $(Cs + Rb)/Th$,
522 7.156 for $(Cs + Rb)/Zr$, and 0.431 for $3K/Al$. Accordingly, $I_N = 1$ represents the local background,
523 whereas values above or below unity indicate relative enrichment or depletion, respectively.

524 **Table 6** shows a simultaneous increase in all three indices between 515.83 and 587.59 m. Outside this
525 interval, $(Cs + Rb)/Zr$ and $3K/Al$ return to values close to or below the local background, whereas
526 $(Cs + Rb)/Th$ retains greater variability.

527 **4.6. Downhole variation in the indices**

528 Within the distal halo, the median values of $(Cs + Rb)/Th$, $(Cs + Rb)/Zr$, and $3K/Al$ are 7.13, 7.16, and
529 0.431, respectively. Their interquartile ranges indicate moderate variability around these values, particularly
530 for the Th- and Zr-normalized ratios. All three indices increase within the proximal transition. Median
531 $(Cs + Rb)/Th$ reaches 12.92, equivalent to 1.81 times the local background, whereas median
532 $(Cs + Rb)/Zr$ increases to 10.51, or 1.47 times the background value. The largest relative change occurs
533 in $3K/Al$, whose median increases to 0.964, equivalent to 2.24 times the distal value.

534 The central domain maintains the enrichment observed in all three indices. Median $(Cs + Rb)/Th$,
535 $(Cs + Rb)/Zr$, and $3K/Al$ values reach 13.49, 13.05, and 0.966, respectively. Their normalized values are
536 1.89, 1.82, and 2.24. The similarity between the proximal transition and the central domain indicates that
537 enrichment extends continuously from 515.83 to 587.59 m. The individual maxima do not occur at precisely
538 the same depths. The $(Cs + Rb)/Th$ ratio reaches 29.08 between 528.60 and 529.18 m; $3K/Al$ reaches a
539 maximum of 1.136 between 546.22 and 546.56 m; and $(Cs + Rb)/Zr$ reaches 20.39 between 551.30 and
540 553.10 m. Nevertheless, all three maxima occur within the corridor encompassing the proximal transition
541 and the central domain.

542 Below 587.73 m, $(Cs + Rb)/Zr$ decreases to 0.86 times the local background in the chlorite halo and 0.83
543 times the background in the peripheral halo. The $3K/Al$ index decreases to 0.88 and 0.96, respectively. In
544 contrast, $(Cs + Rb)/Th$ retains normalized values of 1.17 in the chlorite halo and 1.35 in the peripheral
545 halo. The latter domain contains only four samples and exhibits the widest IQR in the section.

546 **4.7. Differentiation among hydrothermal domains**

547 All three lithogeochemical indices exhibit significant overall differences among the hydrothermal domains.
548 The Kruskal–Wallis test yielded $H = 28.58$ for $(Cs + Rb)/Th$, $H = 23.08$ for $(Cs + Rb)/Zr$, and $H =$
549 26.64 for $3K/Al$, with $p < 0.001$ in all three cases. Effect sizes (ε^2) ranged from 0.285 to 0.367.

550 Dunn's post hoc tests with Holm correction indicate that both the proximal transition and central domain
551 differ significantly from the distal halo. In contrast, the chlorite and peripheral halos do not differ
552 significantly from the distal halo after adjustment for multiple comparisons (**Table 7**).

553

Table 6. Variation in lithogeochemical indices by hydrothermal domain in DDH11025-074

Domain	Interval (m)	n	$(Cs + Rb)/Th$, median [IQR]	$I_{Th,N}$	$(Cs + Rb)/Zr$, median [IQR]	I_{Zr}, N	$3K/Al$, median [IQR]	$I_{3K/Al,N}$
Distal halo	443.80–515.69	15	7.13 [5.84–7.83]	1.04	7.16 [5.59–7.92]	1.05	0.431 [0.391–0.476]	1.06
Proximal transition	515.83–539.70	19	12.92 [8.85–14.05]	1.89	10.51 [7.88–14.24]	1.55	0.964 [0.432–1.081]	2.38
Central domain	539.84–587.59	26	13.49 [11.33–15.25]	1.97	13.05 [10.37–14.56]	1.92	0.966 [0.656–1.107]	2.39
Chlorite halo	587.73–635.47	8	8.34 [6.03–9.61]	1.22	6.19 [5.53–7.72]	0.91	0.379 [0.274–0.561]	0.94
Peripheral halo	635.61–683.35	4	9.62 [7.02–14.16]	1.41	5.94 [3.11–10.48]	0.88	0.414 [0.328–0.458]	1.02

Note. n denotes the number of independent analytical intervals; IQR, interquartile range. The normalized indices correspond to the median value of each domain divided by the median of the distal halo.

Table 7. Statistical comparison of lithogeochemical indices among hydrothermal domains

Statistic or comparison	$(Cs + Rb)/Th$	$(Cs + Rb)/Zr$	$3K/Al$
Kruskal-Wallis statistic (H)	28.58	23.08	26.64
Overall p-value	<0.001	<0.001	<0.001
ε^2	0.367	0.285	0.338
Proximal transition vs. distal halo, p_{Holm}	<0.001	0.030	0.018
Central domain vs. distal halo, p_{Holm}	<0.001	<0.001	<0.001
Outer halos vs. distal halo	Not significant	Not significant	Not significant

Note. Post hoc comparisons were performed using Dunn's test with Holm correction. "Outer halos" comprise the chlorite and peripheral domains. The adopted significance level was $\alpha = 0.05$.

The downhole distributions and statistical contrasts among the hydrothermal domains are presented in **Figs. 9** and **10**. **Fig. 9** shows that the simultaneous occurrence of normalized values above unity is concentrated predominantly between 515.83 and 587.59 m. **Fig. 10** summarizes the domain-specific medians and interquartile ranges and distinguishes the domains that differ significantly from the distal halo.

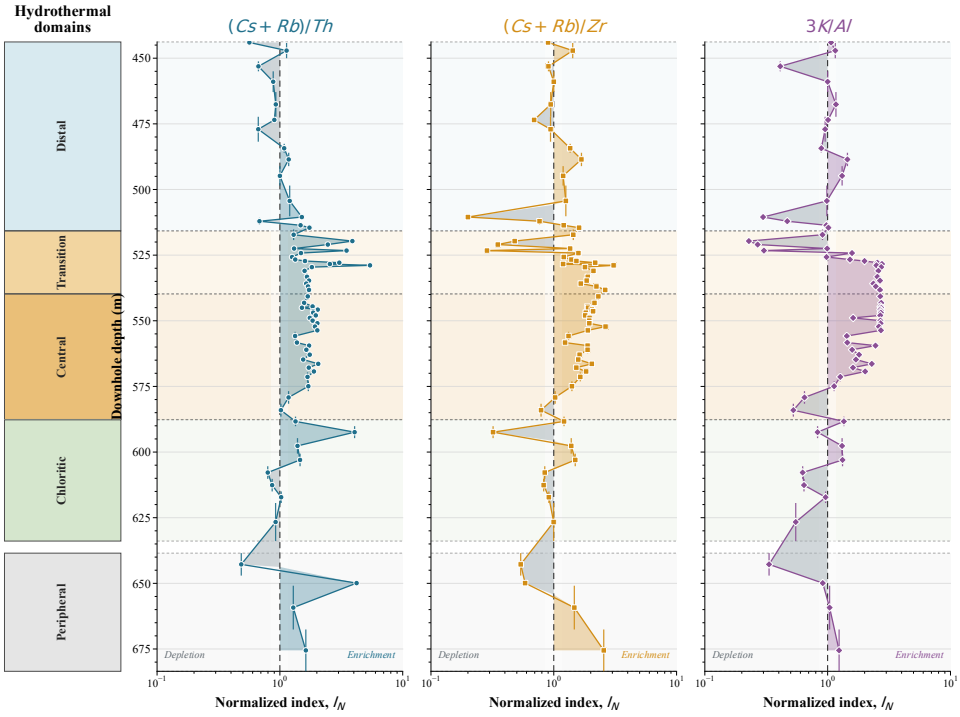


Fig. 9. Downhole variation and statistical differentiation of the lithogeochemical indices in DDH11025-074

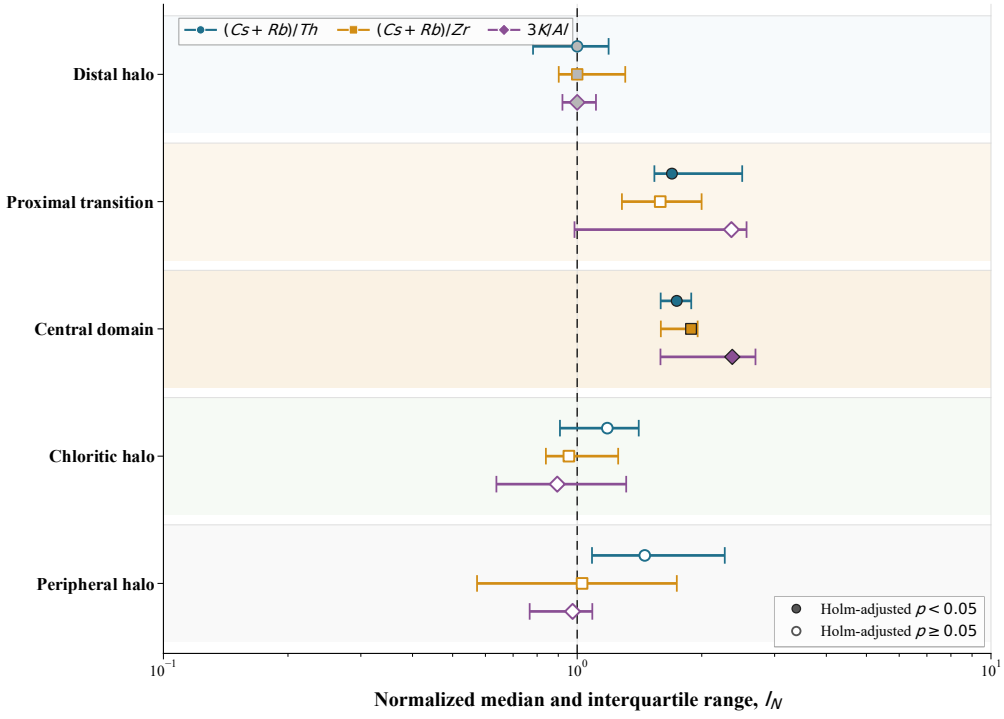


Fig. 10. Normalized medians and interquartile ranges by hydrothermal domain in DDH11025-074

4.8. Statistical relationships among geochemistry, SWIR variables, and mineralization

Statistical relationships were evaluated using 72 independent intervals from DDH11025-074. For DDH11026-081, the 109 spectral records were grouped by analytical sample, yielding 44 independent observations. The p-values were adjusted using the Benjamini–Hochberg procedure, and confidence intervals were calculated from 5,000 bootstrap resamples.

4.8.1. Geochemical and Spectral Relationships in DDH11025-074

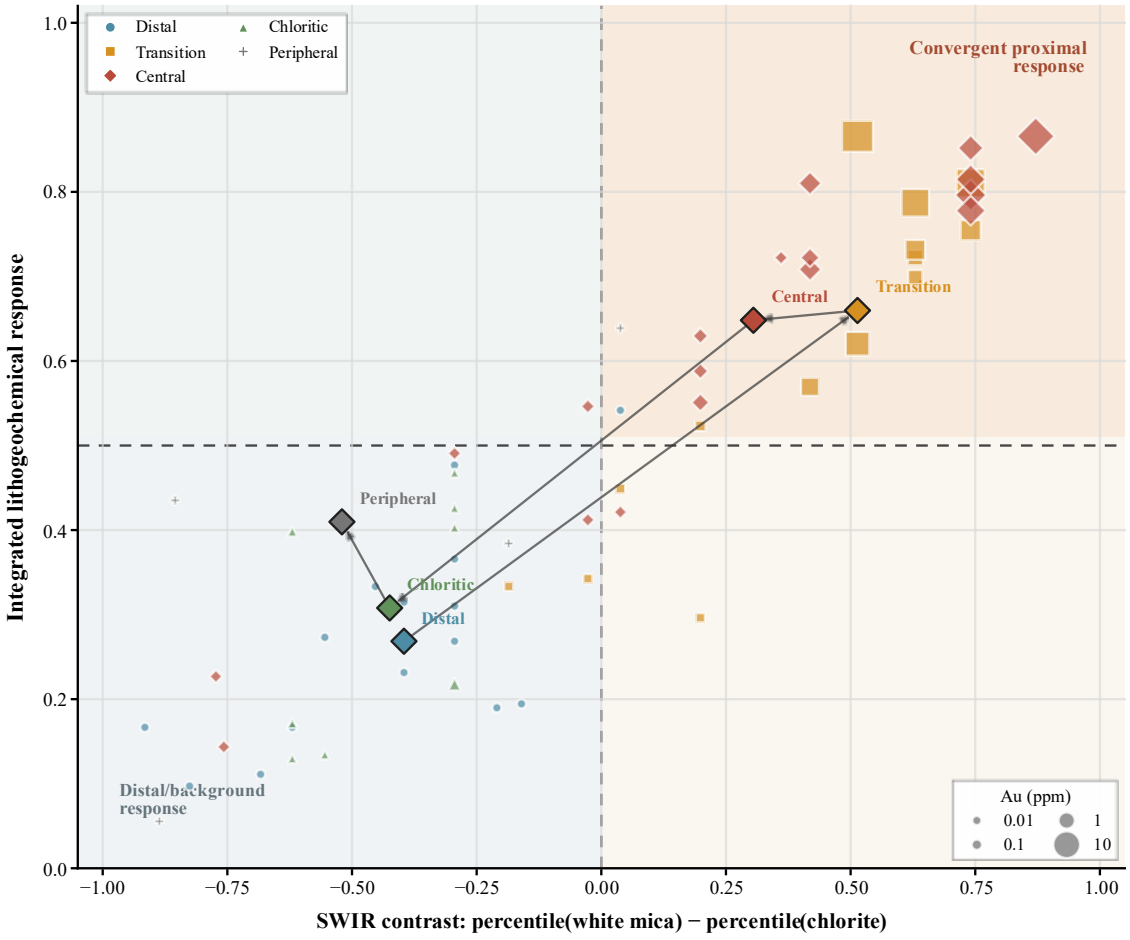
Au exhibits positive correlations with Ag, As, Cu, Pb, and Zn. The strongest association is with As ($\rho_s = 0.895$), followed by Ag ($\rho_s = 0.831$), Pb ($\rho_s = 0.778$), Cu ($\rho_s = 0.715$), and Zn ($\rho_s = 0.650$). All correlations remain significant after correction for multiple comparisons (**Table 8**).

Table 8. Correlations of Au with associated metals, lithogeochemical indices, and SWIR variables in DDH11025-074

Group	Variable	(n)	Spearman's ρ_s	Bootstrap 95% CI	$qFDR$
Metals	As	72	0.895	0.812–0.938	(<0.001)
	Ag	72	0.831	0.712–0.906	(<0.001)
SWIR	White mica (%)	69	0.816	0.682–0.898	(<0.001)
Indices	$(Cs + Rb)/Th$	72	0.807	0.691–0.885	(<0.001)
	$3K/Al$	72	0.793	0.661–0.873	(<0.001)
Metals	Pb	69	0.778	0.634–0.860	(<0.001)
	Cu	72	0.715	0.569–0.818	(<0.001)
Indices	$(Cs + Rb)/Zr$	72	0.711	0.544–0.829	(<0.001)
SWIR	Chlorite (%)	63	−0.684	−0.831–−0.483	(<0.001)
Metals	Zn	70	0.65	0.452–0.803	(<0.001)
	Chlorite absorption wavelength	41	−0.495	−0.729–−0.213	0.001
SWIR	White-mica absorption wavelength	68	0.436	0.186–0.645	(<0.001)
	Carbonates (%)	67	−0.037	−0.282–0.214	0.766

Note. ρ_s, Spearman's rank correlation coefficient; 95% CI, confidence interval obtained from 5,000 bootstrap resamples; q_{FDR}, p-value adjusted using the Benjamini–Hochberg procedure.

White-mica abundance exhibits a strong positive correlation with Au ($\rho_s = 0.816$), whereas chlorite abundance shows an inverse association ($\rho_s = -0.684$). Pos2200 is moderately and positively correlated with Au ($\rho_s = 0.436$). The chlorite absorption wavelength displays a negative relationship of similar magnitude ($\rho_s = -0.495$), although it has more limited analytical coverage ($n = 41$). Carbonate abundance shows no monotonic relationship with Au ($\rho_s = -0.037$; $q = 0.766$). This is the only variable in **Table 8** whose confidence interval broadly spans zero. The graphical integration of the lithogeochemical indices and spectral variables is presented in **Fig. 11**.



589

590 **Fig. 11.** Convergence of the integrated lithogeochemical response, SWIR mineralogical contrast, and Au
591 concentration in DDH11025-074

592 ***4.8.2. Relationships between Au-Ag and SWIR mineralogy in DDH11026-081***

593 In DDH11026-081, Au and Ag exhibit a moderate-to-strong positive correlation ($\rho_s = 0.629$, $p < 0.001$,
594 $n = 44$). Evaluation of the individual mineral scores indicates that phengite is the only phase significantly
595 associated with Au after FDR adjustment (**Table 9**).

596 **Table 9.** Correlations of SWIR mineral scores with Au and Ag in DDH11026-081

SWIR mineral	Samples containing mineral	ρ_s with Au	*qFDR*	ρ_s with Ag	*qFDR*
Phengite	36	0.462	0.01	0.234	0.378
Ankerite	8	0.178	0.371	0.192	0.424
Magnesite	6	0.023	0.88	0.099	0.629
Montmorillonite	8	−0.076	0.747	−0.136	0.567
Siderite	23	−0.192	0.371	−0.335	0.158
Fe-Mg chlorite	7	−0.267	0.238	0.027	0.861

Note. Correlations were calculated using 44 independent analytical samples. Mineral scores represent the mean contribution of each mineral to the spectra collected within each interval. FDR adjustment was applied separately to the six Au correlations and the six Ag correlations.

The phengite score exhibits a moderate positive correlation with Au ($\rho_s = 0.462$, $q = 0.010$) but not with Ag ($\rho_s = 0.234$, $q = 0.378$). Samples containing phengite have a median Au concentration of 0.975 ppm, compared with 0.325 ppm in samples lacking this phase. However, this binary difference does not remain significant after correction for multiple comparisons.

Ankerite, magnesite, and montmorillonite exhibit no significant correlations with either Au or Ag. Fe–Mg chlorite shows a negative trend with Au ($\rho_s = -0.267$), although the result does not reach statistical significance after FDR adjustment. Siderite is negatively correlated with Ag ($\rho_s = -0.335$), but this association also becomes non-significant after FDR adjustment ($q = 0.158$). Figure 12 illustrates the relationship among the aggregated phengite spectral score and Au–Ag concentrations. Samples from the main hydrothermal domain are predominantly concentrated at phengite scores of 0.5–1.0 and encompass the highest Au concentrations recorded in the drill hole.

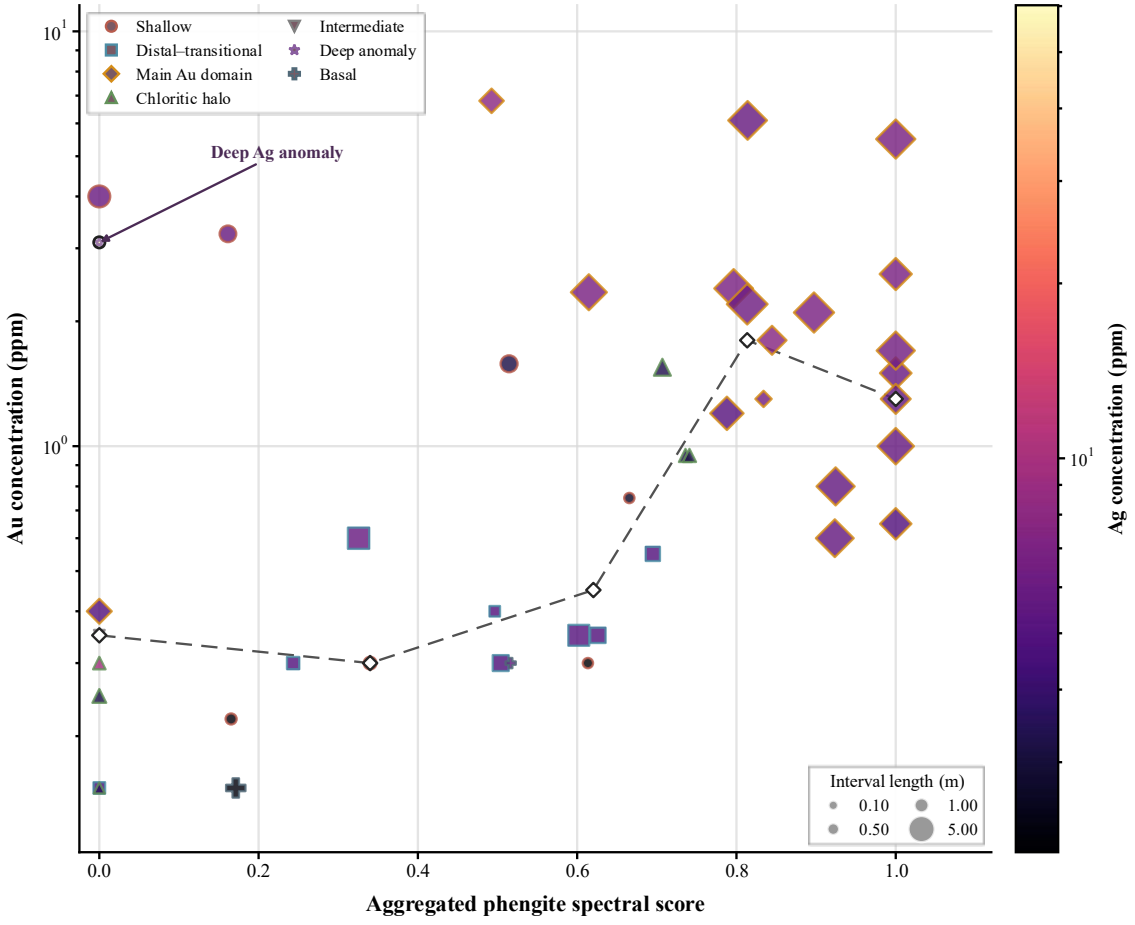


Fig. 12. Relationship between the aggregated phengite spectral score and the distribution of Au–Ag in DDH11026-081

DDH11025-074 exhibits statistical convergence among Au, As, the three lithogeochemical indices, and increasing white-mica abundance, accompanied by decreasing chlorite abundance. In DDH11026-081, the

only significant association is between the continuous phengite score and Au; the remaining mineral phases exhibit no significant monotonic relationships when evaluated individually.

Collectively, the results distinguish three groups of variables:

1. Metal variables associated with Au: As, Ag, Pb, Cu, and Zn.
2. Alteration variables associated with Au: white mica, phengite, $(Cs + Rb)/Th$, $(Cs + Rb)/Zr$, and $3K/Al$.
3. Variables without significant monotonic associations: carbonates in DDH11025-074 and ankerite, magnesite, montmorillonite, and siderite in DDH11026-081.

5. Discussion

The zoning recognized in DDH11025-074 (from chlorite–epidote assemblages toward white mica–illite, followed by a return to chlorite-dominated domains) records the progressive hydrothermal transformation of the host rock around a corridor characterized by enhanced fluid–rock interaction. This configuration is consistent with the proximal white-mica–carbonate–sulfide alteration described in the Pataz gold veins by Haeberlin et al. (2004) and Witt et al. (2014, 2016). In contrast, DDH11026-081 contains a phengite–carbonate core between 523.00 and 558.88 m, accompanied by spatially separated mineralized intervals. This distribution is compatible with heterogeneous structural permeability controlled by fault intersections, changes in strike, and dilational zones, as proposed by Wiemer et al. (2021, 2022) for the Pataz district. However, the contrast between the two drill holes is also influenced by their uneven measurement densities: DDH11025-074 has nearly continuous SWIR coverage, whereas extensive sections of DDH11026-081 are represented by only a few spectra. The available data therefore demonstrate continuous zoning in the first drill hole but only an apparently segmented configuration in the second.

The metal distribution confirms that mineralization is not defined by a single high-grade Au peak but by the superposition of enrichment patterns with differing spatial extents and metal associations. In DDH11025-074, the maximum Au concentration of 31.20 ppm occurs within an approximately 7-m-long proximal interval that also contains clustered Ag, As, Cu, Pb, and Zn maxima. Immediately below, the central domain retains a median Au concentration of 0.419 ppm and persistently elevated As. The correlations of Au with As ($\rho_s = 0.895$), Ag ($\rho_s = 0.831$), Pb ($\rho_s = 0.778$), Cu ($\rho_s = 0.715$), and Zn ($\rho_s = 0.650$) are consistent with a pyrite–arsenopyrite assemblage accompanied by galena, chalcopyrite, and sphalerite, which has been widely documented at Pataz (Haeberlin et al. 2004; Witt et al. 2016). DDH11026-081, in turn, contains a principal domain with a median Au concentration of 1.70 ppm and a deep anomaly containing 3.10 ppm Au and 60.20 ppm Ag. The Ag/Au ratio of 19.42 in the latter contrasts with the median ratio of 4.03 in the principal domain and suggests a distinct metal response. Nevertheless, because it is derived from a single 0.10-m sample, it does not provide sufficient evidence for vertical continuity or a separate mineralizing event. This localized decoupling of Au and Ag is consistent with the strong compartmentalization of fluids and metals that characterizes structurally controlled gold systems (Goldfarb and Pitcairn 2023).

The lithogeochemical indices quantitatively delineate the hydrothermal corridor intersected by DDH11025-074. Relative to the distal halo, normalized median values of $(Cs + Rb)/Th$, $(Cs + Rb)/Zr$, and $3K/Al$

reach 1.81, 1.47, and 2.24, respectively, within the proximal transition, and 1.89, 1.82, and 2.24 within the central domain. Differences among the domains are statistically significant ($p < 0.001$), with effect sizes ranging from 0.285 to 0.367, whereas the outer halos do not differ significantly from the background after Holm correction. At the drill-hole scale, this behavior is consistent with the findings of Heath and Campbell (2004) and Witt et al. (2014): Cs–Rb-based ratios record alkali-element redistribution, whereas $3K/Al$ responds more selectively to the development of white mica. However, the isolated increase in $(Cs + Rb)/Th$ within the peripheral halo, without corresponding increases in $(Cs + Rb)/Zr$ and $3K/Al$, demonstrates that an individual ratio may be affected by variations in protolith composition or accessory-mineral abundance. This limitation agrees with Bacha et al. (2021), who emphasized that the exploration utility of Rb and Cs depends on the lithological context.

The statistical integration of geochemical and spectroscopic data demonstrates that effective vectoring depends on continuous mineralogical associations rather than the isolated occurrence of a single phase. In DDH11025-074, Au is positively correlated with white-mica abundance ($\rho_s = 0.816$) and the three lithogeochemical indices ($\rho_s = 0.711$–0.807), but inversely correlated with chlorite abundance ($\rho_s = -0.684$). Pos2200 exhibits a weaker association with Au ($\rho_s = 0.436$), whereas carbonate abundance shows no significant monotonic relationship. These contrasting responses explain why the direction of the Al–OH wavelength shift should not be transferred directly among deposits: longer wavelengths were interpreted as proximal indicators at Xiaonangou and Tengjia, whereas shifts toward shorter wavelengths were documented at Mailong and Jinwozi; at Jiaojia, Pos2200 did not display consistent spatial zoning (Hao et al. 2024; H. Wang et al. 2024, 2025; M. Wang et al. 2024; Y. Wang et al. 2025). In DDH11026-081, only the continuous phengite score retains a significant association with Au after FDR adjustment ($\rho_s = 0.462$), whereas the simple presence or absence of phengite is not discriminatory. Collectively, these results support an empirical model in which the most reliable vector is defined by the coupled increase in white mica–phengite, Cs–Rb enrichment, and $3K/Al$, accompanied by decreasing chlorite abundance and independently validated by Au–As enrichment. This convergence provides a more reproducible signal than any mineral, geochemical index, or spectral parameter considered separately.

6. Conclusions

The integration of multielement geochemistry and SWIR spectroscopy enabled the identification of complementary vectors toward gold mineralization in the investigated drill holes. In DDH11025-074, the 515.83–587.59 m hydrothermal corridor is characterized by simultaneous increases in $(Cs + Rb)/Th$, $(Cs + Rb)/Zr$, and $3K/Al$, together with increasing white-mica abundance and decreasing chlorite abundance. These indicators exhibit significant associations with Au, particularly white-mica abundance ($\rho_s = 0.816$) and the lithogeochemical indices ($\rho_s = 0.711$–0.807), whereas As is the metal most strongly associated with gold mineralization ($\rho_s = 0.895$). In DDH11026-081, the phengite spectral score is also positively associated with Au ($\rho_s = 0.462$), although within a more segmented hydrothermal architecture characterized by uneven spectral coverage. The most robust vector is therefore not defined by an individual mineral, geochemical ratio, or isolated maximum value, but by the spatial convergence of Cs–Rb and K enrichment, increasing white mica–phengite abundance, decreasing chlorite abundance, and a coupled Au–As response.

The scope of the proposed model is limited by the small number of drill holes, the availability of multielement geochemical data only for DDH11025-074, the selective distribution of SWIR measurements in DDH11026-081, and the absence of independent mineralogical validation through X-ray diffraction or mineral chemistry. The values identified herein should therefore be regarded as local empirical references rather than universal thresholds directly transferable across the entire Pataz Batholith. Nevertheless, this approach provides a reproducible framework for prioritizing drill intervals in which geological, geochemical, and spectral evidence converges, thereby reducing reliance on visual indicators or isolated assay values. Future research should validate the model using a larger number of drill holes and lithological units, incorporate Pos2200, absorption-band depth, and crystallinity indices derived directly from the spectra, and compare SWIR variations with X-ray diffraction, petrography, and in situ chemical analyses of white mica and chlorite.

DECLARATIONS

Funding

The authors declare that no funds, grants, or other support were received during the preparation of this manuscript.

Competing Interests

The authors have no relevant financial or non-financial interests to disclose.

Author Contributions

All authors contributed to the conception and design of the study. Clever Willam Caruajulca-Caruajulca, Roy Edinson Coba-Teran, and Carlos Ore-Sanchez contributed to geological logging, drill-core characterization, data acquisition, and geological interpretation. José Néstor Mamani-Quispe contributed to analytical and methodological support and interpretation of the geochemical results. Jairo Jhonatan Marquina-Araujo performed data processing, statistical analysis, visualization, integration of the geological, geochemical, and SWIR datasets, interpretation of results, and preparation of the first draft of the manuscript. Marco Antonio Cotrina-Teatino contributed to the study methodology, research supervision, interpretation of results, and critical review of the manuscript. Jose Saavedra-Rosas contributed to the validation and interpretation of the geological and geochemical results and critically reviewed the manuscript. Salomon Ortiz-Quintanilla contributed to the interpretation and validation of the SWIR spectral results and to the critical review of the manuscript. José A. Guartan contributed to the geological interpretation, validation of the integrated results, and critical review of the manuscript. All authors critically revised previous versions of the manuscript, read, and approved the final version.

Data Availability

The geological logging, geochemical assay results, and SWIR spectral data analysed during the current study are associated with an operating mining project and are not publicly available because they contain proprietary information. The data may be made available by the corresponding author upon reasonable request and subject to authorization from the data owner.

Code Availability

No custom code or software application was developed for this study. Data processing and analyses were performed using the analytical procedures and software described in the Materials and Methods section.

References

ALS global. (2023) Four-Acid Digest & Advanced ICP-MS Technology.

Bacha RRB, Toledo CLB, Silva AM, Mungall JE (2021) Alkali element mobility as a vector for gold mineralization: An example from Central Brazil. *Geochemistry* 81(4) https://doi.org/10.1016/j.chemer.2021.125808

Cloutier J, Piercey SJ, Huntington J (2021) Mineralogy, mineral chemistry and swir spectral reflectance of chlorite and white mica. *Minerals* 11(5) https://doi.org/10.3390/min11050471

Dominy SC, Edgar WB (2012) Approaches to reporting grade uncertainty in high nugget gold veins. *Transactions of the Institutions of Mining and Metallurgy, Section B: Applied Earth Science* 121(1) https://doi.org/10.1179/1743275812Y.0000000013

Dominy SC, Platten IM, Raine MD (2003) Grade and geological continuity in high-nugget effect gold-quartz reefs: Implications for resource estimation and reporting. *Transactions of the Institution of Mining and Metallurgy, Section B: Applied Earth Science* 112(3) https://doi.org/10.1179/037174503225003116

Gaillard N, Williams-Jones AE, Clark JR, Lypaczewski P, Salvi S, Perrouty S, et al. (2018) Mica composition as a vector to gold mineralization: Deciphering hydrothermal and metamorphic effects in the Malartic district, Quebec. *Ore Geology Reviews* 95 https://doi.org/10.1016/j.oregeorev.2018.02.009

Goldfarb RJ, Groves DI, Gardoll S (2001) Orogenic gold and geologic time: A global synthesis. *Ore Geology Reviews* 18(1–2) https://doi.org/10.1016/S0169-1368(01)00016-6

Goldfarb RJ, Pitcairn I (2023) Orogenic gold: is a genetic association with magmatism realistic? *Mineralium Deposita* 58(1) https://doi.org/10.1007/s00126-022-01146-8

Groves DI, Santosh M, Goldfarb RJ, Zhang L (2018) Structural geometry of orogenic gold deposits: Implications for exploration of world-class and giant deposits. *Geoscience Frontiers* 9(4) https://doi.org/10.1016/j.gsf.2018.01.006

Haeberlin Y, Moritz R, Fontboté L, Cosca M (2004) Carboniferous orogenic gold deposits at Pataz, Eastern Andean Cordillera, Peru: Geological and structural framework, paragenesis, alteration, and 40Ar/39Ar geochronology. *Economic Geology* 99(1) https://doi.org/10.2113/gsecongeo.99.1.73

Hao J, Duan L, Zhang Y, Zhao H, Shao Y, Guo Y, et al. (2024) Machine learning on white mica short-wave infrared (SWIR) spectral data in the Tengjia Au deposit, Jiaodong peninsula (Eastern China): A

prospecting indicator for lode gold deposits. *Ore Geology Reviews* 173 https://doi.org/10.1016/j.oregeorev.2024.106230

Heath CJ, Campbell IH (2004) A new geochemical technique for gold exploration: Alkali element mobility associated with gold mineralization in the West Australian Goldfields. *Economic Geology* 99(2) https://doi.org/10.2113/gsecongeo.99.2.313

Liu L, Chen J, Li X, Zhou T, Li S, Sun L, et al. (2024) Short wavelength infrared (SWIR) reflectance spectroscopy of alteration minerals of Qibaoshan ore district, Shandong Province, China. *Ore Geology Reviews* 165 https://doi.org/10.1016/j.oregeorev.2024.105868

Liu YH, Wang R, Zhou DY, Zhao Y (2026) White mica as an exploration vector for Archean gold deposits: Integration of in-situ chemistry and SWIR spectroscopy at Kanowna Belle and Sunrise Dam, Western Australia. *Journal of Geochemical Exploration* 289:108143 https://doi.org/10.1016/j.gexplo.2026.108143

Lypaczewski P, Rivard B, Gaillard N, Perrouty S, Piette-Lauzière N, Bérubé CL, Linnen RL (2019) Using hyperspectral imaging to vector towards mineralization at the Canadian Malartic gold deposit, Québec, Canada. *Ore Geology Reviews* 111 https://doi.org/10.1016/j.oregeorev.2019.102945

Medina CM, Ducart DF, Passos JS, de Oliveira LR (2021) Exploration vectoring from the white mica spectral footprint in the atypical auriferous Lavra Velha deposit, San Francisco Craton, Brazil. *Ore Geology Reviews* 139 https://doi.org/10.1016/j.oregeorev.2021.104438

Meyer JM, Kokaly RF, Holley E (2022) Hyperspectral remote sensing of white mica: A review of imaging and point-based spectrometer studies for mineral resources, with spectrometer design considerations. *Remote Sensing of Environment.* https://doi.org/10.1016/j.rse.2022.113000

Salama W, Goswami N, Lampinen H, Verrall M, Schoneveld L (2025) Mapping hydrothermal alteration in regolith using white micas and chlorite as vectors towards gold mineralization. *Journal of Geochemical Exploration* 268 https://doi.org/10.1016/j.gexplo.2024.107603

Sweetapple MT, Vanstone PJ, Lumpkin GR, Collins PLF (2024) A review of lithogeochemical dispersion haloes of LCT pegmatites, and their application to rare metal exploration, with special reference to lithium in an Australian context. *Australian Journal of Earth Sciences.* https://doi.org/10.1080/08120099.2024.2379834

Thiele ST, Kirsch M, Lorenz S, Saffi H, El Alami S, Contreras Acosta IC, et al. (2024) Maximising the value of hyperspectral drill core scanning through real-time processing and analysis. *Frontiers in Earth Science* 12 https://doi.org/10.3389/feart.2024.1433662

Wang H, Sun W, Li H, Yu X, Gu C, Ma C, et al. (2024) Application of geological and short wavelength infrared (SWIR) spectroscopy mapping in the Mailong gold deposit, East Kunlun: Implications for exploration targeting. *Ore Geology Reviews* 169 https://doi.org/10.1016/j.oregeorev.2024.106080

Wang H, Zhang J, Ding Z, Zhang Q, Zhao J (2025) Short wavelength infrared (SWIR) of white micas as a vectoring exploration tool for the Jiaojia gold deposit, Jiaodong Peninsula: implications for district- to deposit-scale gold exploration. *Ore Geology Reviews* 181 https://doi.org/10.1016/j.oregeorev.2025.106626

Wang M, Mao J, Wang Z, Yan G, Liu S, Jiang H, et al. (2024) Short wavelength infrared (SWIR) spectral and geochemical characteristics of white micas in the Xiaonangou gold deposit, East Qinling: As a hyperspectral tool in exploration. *Ore Geology Reviews* 175 https://doi.org/10.1016/j.oregeorev.2024.106349

Wang Y, Xiao B, Wang Y, Zhao J, Wang H, Cao G (2025) Hydrothermal alteration and shortwave infrared (SWIR) spectroscopy exploration of the Jinwozi gold deposit in the Beishan Orogenic Belt, NW China. *Ore Geology Reviews* 185 https://doi.org/10.1016/j.oregeorev.2025.106820

Wang Z, Zhang X, Sun Y, Geng Y, Huang G, Zhang M, et al. (2026) Application of white mica minerals to exploration of orogenic gold deposit: A case study of Wuzunbulake gold deposit, South Tianshan (NW China). *Journal of Geochemical Exploration* 282 https://doi.org/10.1016/j.gexplo.2025.107957

Wiemer D, Hagemann SG, Hronsky J, Kemp AIS, Thébaud N, Ireland T, Villanes C (2022) Ancient structural inheritance explains gold deposit clustering in northern Perú. *Geology* 50(10) https://doi.org/10.1130/G50208.1

Wiemer D, Hagemann SG, Thébaud N, Villanes C (2021) Role of basement structural inheritance and strike-slip fault dynamics in the formation of the pataz gold vein system, Eastern Andean Cordillera, Northern Peru. *Economic Geology* 116(7) https://doi.org/10.5382/econgeo.4839

Witt WK, Hagemann SG, Ojala J, Laukamp C, Vennemann T, Villanes C, Nykanen V (2014) Multiple methods for regional- to mine-scale targeting, Pataz gold field, northern Peru. *Australian Journal of Earth Sciences* 61(1) https://doi.org/10.1080/08120099.2013.763859

Witt WK, Hagemann SG, Villanes C, Vennemann T, Zwingmann H, Laukamp C, Spangenberg JE (2016) Multiple gold mineralizing styles in the Northern Pataz District, Peru. *Economic Geology* 111(2) https://doi.org/10.2113/econgeo.111.2.355

Witt WK, Hagemann SG, Villanes C, Zeng Q (2013) New geochronological results and structural evolution of the Pataz gold mining district: Implications for the timing and origin of the batholith-hosted veins. *Ore Geology Reviews* 50 https://doi.org/10.1016/j.oregeorev.2012.10.007

Zhao H, Duan L, Zhang Y, Han X, Shao Y, Pan Y, et al. (2026) Optimizing short-wave infrared (SWIR) indications of alteration minerals for deep mineralization exploration in the Qianchuiliu lode gold deposit, Jiaodong Peninsula. *Journal of Geochemical Exploration* 282 https://doi.org/10.1016/j.gexplo.2025.107966